

Colour Evolution of Disk Galaxy Models from $z=4$ to $z=0$

P. Westera¹, M. Samland¹, R. Buser¹, and O. E. Gerhard¹

Astronomisches Institut der Universität Basel, Venusstrasse 7, CH-4102 Binningen, Switzerland
e-mail: samland@astro.unibas.ch, westera@astro.unibas.ch

Received ;date; accepted ;date;

Abstract. We calculate synthetic *UBVRIJHKLM* images, integrated spectra and colours for the disk galaxy formation models of Samland & Gerhard (2002), from redshift $z = 4$ to $z = 0$. Two models are considered, an accretion model based on Λ CDM structure formation simulations, and a classical collapse model in a dark matter halo. Both models provide the star formation history and dynamics of the baryonic component within a three-dimensional chemo-dynamical description. To convert to spectra and colours, we use the latest, metallicity-calibrated spectral library of Westera et al. (2002), including internal absorption. As a first application, we compare the derived colours with Hubble Deep Field North bulge colours and find good agreement. With our model, we disentangle metallicity effects and absorption effects on the integrated colours, and find that absorption effects are dominant for $z < 1.5$. Furthermore, we confirm the quality of m_K as a mass tracer, and find indications for a correlation between $(J - K)_0$ and metallicity gradients.

Key words. Galaxies: abundances – Galaxies: evolution – Galaxies: photometry – Galaxies: spiral – dust, extinction

1. Introduction

Today, it is possible to observe galaxies out to high redshift and to study how they form and evolve. Long exposures in different wavelength bands result in images with very faint limiting magnitudes, such as the Hubble Deep Field (HDF Williams et al., 1996) and its NICMOS counterpart (Thompson et al., 1999), or the FORS deep field (Appenzeller et al., 2000), to name but a few. In these deep fields, we can see galaxies back to epochs shortly after their formation. Together with ground-based observations, these data provide morphological and photometric information on the evolution of disk galaxies as a function of redshift (Vogt et al., 1996; Roche et al., 1998; Lilly et al., 1998; Simard et al., 1999). At redshifts $z > 2$, the deep fields reveal a wide range of galactic morphologies with considerable substructure and clumpiness (Pentericci et al., 2001). From redshift $z = 2$ to $z = 1$, massive galaxies seem to assemble (Kajisawa & Yamada, 2001), while for $z < 1$ most of the Hubble type galaxies show only little or no evolution (Lilly et al., 1998). These results are obtained from still small samples of galaxies, but with the new large telescopes much more information about high redshift galaxies will be available in the future.

However, for understanding of the galaxy formation process also theoretical models are needed. Modern galaxy formation models, based on the hierarchical structure formation scenario, predict halo formation histories and

the assembly of the baryonic matter inside these halos (Nagamine et al., 2001; Pearce et al., 2001; Cole et al., 2000; Navarro & Steinmetz, 2000; Hultman & Pharasyn, 1999), but the spatial resolution of these simulations is not sufficient to describe the formation of galaxies in detail. This can be done either in the framework of semi-analytical models (Cole et al., 2000; Firmani & Avila-Reese, 2000; Diaferio et al., 1999; Mo et al., 1998), with hybrid models (Bossier & Prantzos, 2001; Jimenez et al., 1998) or with dynamical models that simulate the formation and evolution of single galaxies (Bekki & Chiba, 2001; Williams & Nelson, 2001; Berczik, 1999; Samland et al., 1997; Steinmetz & Müller, 1995a; Katz & Gunn, 1991). In order to compare the models with the colours and magnitudes of real galaxies, realistic transformations of the models into spectral properties are needed. Only through transformation into spectra and colours, can the galactic models be compared with observations and thereby be confirmed or refined.

Recent applications of such transformations include Gronwall & Koo (1995), who use the Bruzual & Charlot (1993) Galaxy Isochrone Spectral Synthesis Evolution Library (GISSEL93) code to derive integrated spectra for their models of galaxies of different spectral type, and then obtain final spectral energy distributions by adding a simple reddening with a constant E_{B-V} of 0.1. The GISSEL93 code was also used by Roche et al. (1996) for their non-evolving and pure luminosity evolution models of different galaxy types, but they use an absorption coeffi-

cient that is proportional to the star formation rate (SFR) divided by the galaxy mass. Campos & Shanks (1997) also use the GISSEL93 code and a constant absorption for their spiral and early type luminosity evolution models. To take account of the cosmology, they used the K corrections of Metcalfe et al. (1991). The 1999 version of GISSEL, combined with the BaSeL 2.2 (Lejeune et al., 1997, 1998) semi-empirical stellar spectral energy distribution (SED) library was used by Kauffmann & Charlot (1998a,b) for their semi-analytical models. Jimenez et al. (1998, 1999) use their own isochrones and Kurucz 1992 (Buser & Kurucz, 1992) SEDs, complemented with atmosphere models of their own, in their low surface brightness disk galaxy models. Contardo et al. (1998) interpolate the colour evolution of the underlying stars from a grid of theoretical colour evolutionary tracks and then apply a K correction. In all these models no correction for internal dust absorption is made.

In this paper, we combine the disk galaxy formation models of Samland & Gerhard (2002) with the latest metallicity-calibrated stellar SED library (Westera et al., 2002) and galaxy evolutionary code (Bruzual & Charlot, 2000), including the spatially resolved internal absorption obtained from the three-dimensional distribution of gas in these models. We obtain *UBVRIJHKLM* images and spectra (intrinsic and redshifted) of the model galaxies. The redshifted spectra include the Lyman line blanketing and Lyman continuum absorption by absorption systems at cosmological distances using the formulae given by Madau (1995). Comparison of the model galaxies with bulge observations in the Hubble Deep Field North (HDF-N) shows good agreement, confirming our approach. We can disentangle different effects on the spectral properties of a model galaxy, such as from metallicity and internal absorption, by artificially blinding these contributions out, and then recalculating the spectral properties.

The outline of the paper is as follows: In Section 2, the galaxy models are briefly described (for a detailed description, see Samland & Gerhard, 2002). In Section 3, we discuss the programme used for the transformation into colours and spectra, and in Section 4, we present our first results and a comparisons with empirical (HDF-N) data. In the last section, conclusions are drawn, and an outlook on further work is given.

2. Short description of the new galaxy evolution models

The observations of high redshift galaxies of interest here provide magnitudes, colours and some information about morphology (asymmetry and concentration parameter). Interpreting these data fully requires detailed models for galactic evolution. In this paper, we want to show, that a dynamical multi-phase galaxy model provides the necessary physical information to interpret the high redshift data. For this purpose, we use the 3-dimensional chemodynamical models described in detail in the companion paper (Samland & Gerhard, 2002). Here, we only summa-

rize briefly their main properties. These models include cosmological initial conditions, dark matter, stars and the different phases of the interstellar medium (ISM), as well as the feedback processes which connect the ISM and the stars.

We use two different models, both describing the formation and evolution of a disk galaxy in a Λ CDM universe ($H_0 = 70$ km/s/Mpc, $\Omega_0 = 0.3$, $\Omega_\Lambda = 0.7$, and $M_{baryon}/M_{dark} = 1/5$). The spin parameters of the model galaxies are chosen to be $\lambda = 0.05$ (Gardner, 2001; van den Bosch, 1998; Cole & Lacey, 1996; Steinmetz & Bartelmann, 1995b; Barnes & Efstathiou, 1987) and we follow the evolution of both models from $z = 4.85$ (corresponding in this cosmology to a universal age of 1.2 Gyr) until $z = 0$ (13.5 Gyr).

The first model, which we call the collapse model, is an extreme case which starts with an extended halo of 250 kpc radius and which has a total mass of $1.8 \cdot 10^{12} M_\odot$. Initially the baryonic and dark matter is distributed according to the density profile proposed by Navarro et al. (1995). We assume that only the baryonic matter can collapse, similar to an Eggen, Lynden-Bell, and Sandage scenario (Eggen et al., 1962). We use this model mainly as a reference to highlight the differences to a second more realistic, cosmologically motivated model.

This second model, from now on called the accretion model, is characterized by a slowly growing dark halo with a continuous gas and dark matter infall. The time dependent accretion rate is derived by averaging 96 halo merging histories from cosmological N-body simulations from the VIRGO-GIF project (Kauffmann et al., 1999). In this scenario, the dark halo grows slowly from a radius of 15 kpc at $z = 4.85$ to 250 kpc at $z = 0$. We assume that, at $z = 4.85$, the baryonic matter outside the r_{200} radius consists of ionized primordial gas. The accreted gas can cool, forms clouds, dissipates kinetic energy and finally collapses inside the dark halo. The collapse is delayed by the feedback processes and a galaxy with an extended disk forms. This is in agreement with the result of Weil et al. (1989), that the formation of disc galaxies requires feedback processes which prevent gas from collapsing until late epochs.

In the collapse model, the infall of baryonic matter into the innermost 20 kpc of the dark halo is determined only by dissipation and feedback processes between stars and ISM. The black line in Fig. 1 represents the baryonic mass flow into resp. out of a sphere of 20 kpc radius surrounding the model galaxy centre. The collapse model shows an early mass infall that ends more or less at $z = 1$. Later there is some in and outflow, but this does not change the mass of the galaxy significantly. As this 20 kpc region is responsible for most of the star formation (SF), the total SFR (Fig. 2, upper left panel) is strongly correlated with the collapse time, and thus peaks very early at $z \simeq 2$ (corresponding to an age of ~ 3 Gyr). The modest SF from $z = 1$ until the present epoch, is maintained by the gas return from long lived main sequence stars entering the planetary nebula phase. For the colour evolution of a galaxy it is important to know the SF and the enrichment

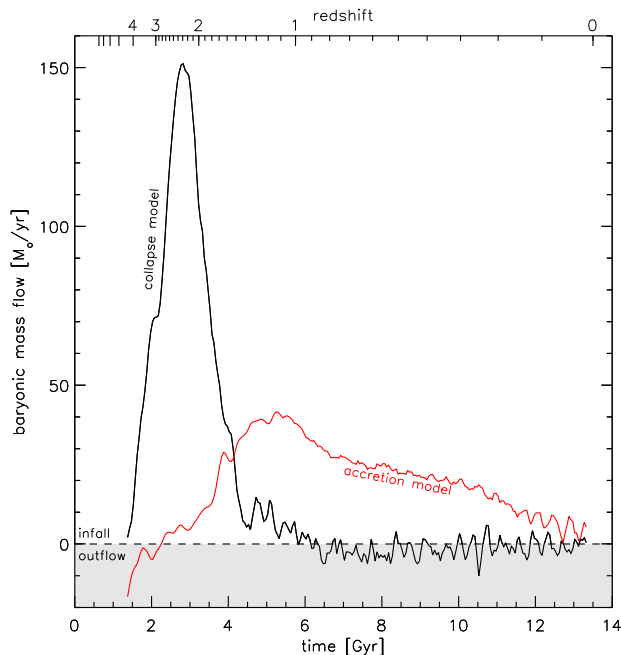


Fig. 1. Baryonic mass flow into resp. out of a sphere of 20 kpc radius surrounding the galaxy centres of the accretion and the collapse models. Negative mass flows (grey shaded region) correspond to net outflows.

history. The lower left panel of Fig. 2 shows the metallicity distribution and the average metallicity of the stellar particles as a function of the time when they were born. In the first ~ 1.5 Gyr of the simulation, the metallicity shoots up from ~ -4 dex to around solar. From this point on, it stays constant, reaching not much more than ~ 0.1 dex at the present epoch. This can be explained by the fact that after the first ~ 1.5 Gyr, the bulk of the SF, and hence of the gas enrichment, is completed. Morphologically, the outcome of the collapse model is an early-type disk galaxy.

In the accretion model, the galaxy forms in a smoother way. The mass flow into the inner 20 kpc is shown in Fig. 1 by the grey (in the colour version: red) line. It has a maximum at $z = 1.1$, but remains significant until the present epoch, because of the steady accretion of baryonic (and dark) matter. Therefore, we expect a larger mixture of stellar populations of many different ages and metallicities, compared to the collapse model. The SFR in the accretion model (Fig. 2, upper right panel) peaks at around $z = 1$ (~ 5.75 Gyr after the big bang), and stays high until $z = 0$. In analogy to the collapse model, the average stellar particle metallicity $[\text{Fe}/\text{H}]$ of this model (shown in the lower right panel of Figure 2) increases most steeply during the phase of maximum SF. It also starts at $[\text{Fe}/\text{H}] \simeq -4$, and reaches its present value of ~ -0.1 dex at $z \simeq 1$. The accretion model galaxy forms from inside-out and from top-to-bottom, with the halo as the oldest component, followed by the bulge and the disk. At $z = 1$, the galaxy begins to form a bar which later turns into a triaxial bulge. This model nicely produces a barred disk galaxy, and since it uses more realistic cosmological initial

conditions, we shall in the following concentrate on this model.

Fig. 3 shows the radial profile of the (stellar) mass surface density, the ages of the stellar particles, and the stellar metallicity, at four redshifts ($z = 1.382, 0.642, 0.252$ and 0 , corresponding to universe ages of 4.5, 7.5, 10.5 and 13.5 Gyr). The profiles (the lines in Fig. 3) were calculated by first projecting the respective quantities on the disk plane, then determining the point of the highest (stellar) mass concentration in this projection, and in the end averaging (mass-weighted) the projections over rings surrounding this point. To show the spread in stellar particle age and metallicity, a representative sample of stellar particles is shown as dots.

In the surface density profile, one can see a clear bulge and a bump appearing at around 6 Gyr at a radius of ~ 10 kpc, indicative of the bar (Lerner et al., 1999; Efstathiou et al., 1982). These features are clearly visible in the images in Section 4. In stellar age, not much of a radial dependence can be seen, apart maybe from a small negative gradient in the inner region, whose outer limit (thus the minimum) slowly wanders outwards from 8 kpc at $z = 0.642$ to 20 kpc today, due to an inside-out forming disk. In metallicity, there is an evident negative gradient, that stays nearly constant from $z = 0.6$ on. This is due to a combination of the metallicity gradient of the disk, which, due the redistribution from the bar, is flat out to ~ 10 kpc (hence the bump there) and drops further outwards, and the shallow halo gradient. More quantitatively, the average metallicity reaches solar in the centre, with the most metal-rich stellar particles reaching $[\text{Fe}/\text{H}] = +0.3$ while at 40 kpc from the centre, the average metallicity has dropped to $[\text{Fe}/\text{H}] \simeq -1$. The important results which we need in Subsection 4.4 are:

1. The surface density drops with radius at all times, and from $z = 0.6$ on, a very steep gradient in the inner few kpc and a bump at around 10 kpc reflect the existence of a bulge and a bar.
2. The stellar age distribution shows almost no gradient.
3. The metallicity drops with increasing projected radius, also showing a bump at around 10 kpc.

The output quantities of interest (which are the input quantities for the programme which calculates the spectral properties) are the following: 614500 stellar particles, each with its position in x , y , and z , initial mass, age, and metallicity, as well as the gas density on a three-dimensional grid covering the galaxy out to where the gas density is negligible (100 kpc). We use the gas density to calculate the internal dust absorption in the model (Section 3). All quantities are followed during the whole galactic evolution. With these data we determine the evolution of the brightness, colours, metallicities and the structure of the model galaxy. In comparison with the observations, we can use the results to interpret the high redshift data but also to improve the galactic models and to learn more about the processes that strongly influence the galactic evolution.

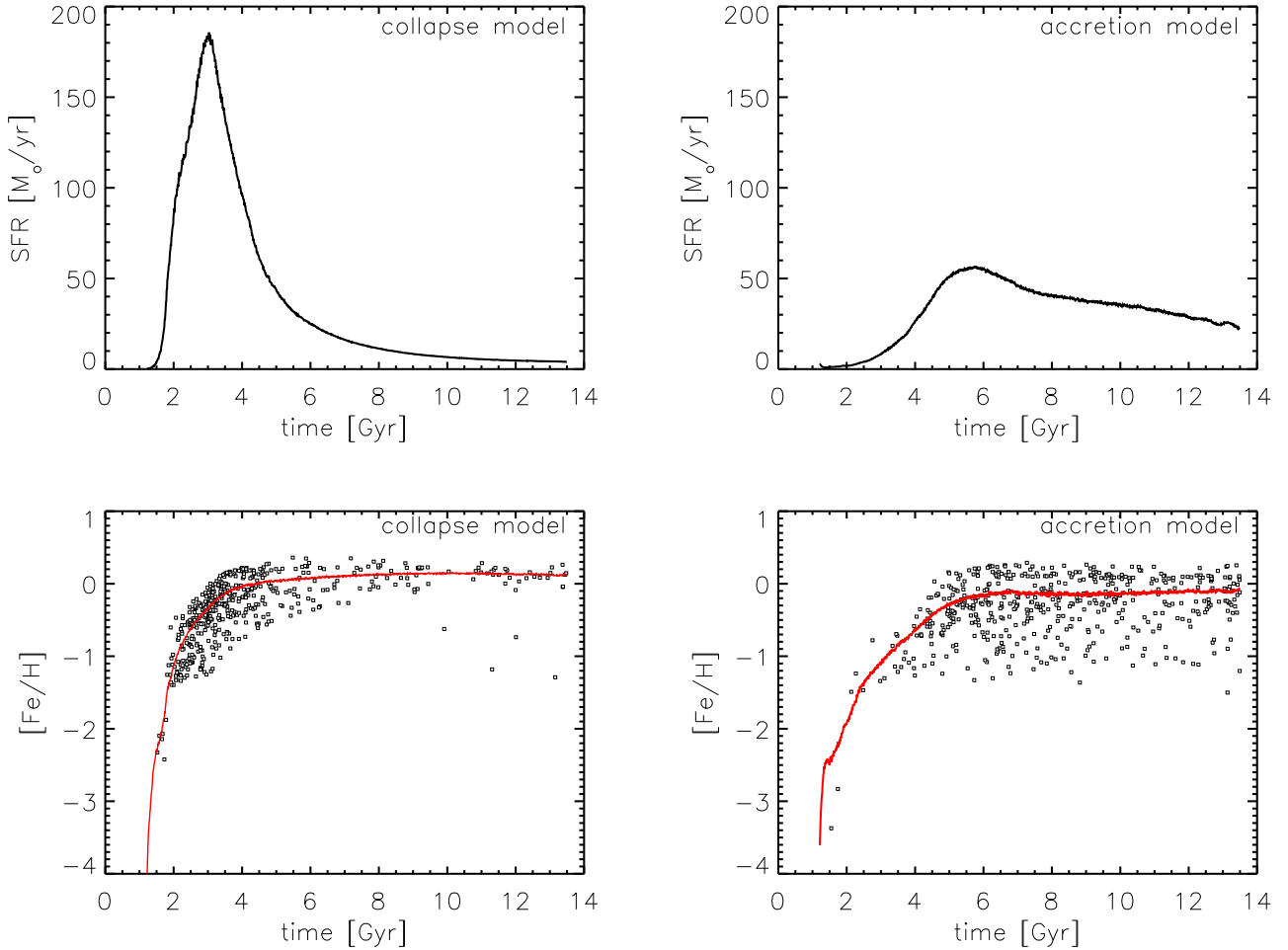


Fig. 2. Upper panels: the star formation rates of the collapse model (left), and the accretion model (right). Lower panels: the age-metallicity distributions and average metallicities of the stellar particles. The small squares show a representative sample of stellar particles.

3. From theoretical quantities to colours and spectra

To derive 2-dimensional colour ($UBVRIJHKLM$) images from the distributions of stars and gas, we proceeded in the following way:

First, a library of simple stellar population (SSP) spectra was produced. With the Bruzual and Charlot 2000 Galaxy Isochrone Spectral Synthesis Evolution Library (GISSEL) code (Charlot & Bruzual, 1991; Bruzual & Charlot, 1993, 2000), integrated spectra (ISEDs) of populations were calculated for a grid of population parameters consisting of 8 metallicities ($[\text{Fe}/\text{H}] = -2.252, -1.65, -1.25, -0.65, -0.35, 0.027, 0.225, \text{ and } 0.748$) and 221 SSP ages ranging from 0 to 20 Gyr. As input, we used Padova 2000 isochrones (Girardi et al., 2000). For the highest and the lowest metallicity, where no Padova 2000 isochrones are available, we used Padova 1995 isochrones (Fagotto et al., 1994; Girardi et al., 1996). The spectral library used was the BaSeL 3.1 "Padova 2000" (Westera et al., 2002; Westera, 2001) stellar library. This library is able

to reproduce globular cluster colour-magnitude diagrams in combination with the Padova 2000 isochrones for all metallicities from $[\text{Fe}/\text{H}] = -2.0$ to 0.5, because it was calibrated (in a metallicity-dependent way) for this purpose, and does a similarly good performance on integrated SSP spectra. Colour differences with template empirical spectra from Bica (1996) amount to a few 100th of a magnitude only (Westera et al., 2002; Westera, 2001). A Salpeter initial mass function (IMF) with cutoff masses of $0.1 M_{\odot}$ and $50 M_{\odot}$ was chosen in accordance with the galaxy models. The spectra of this ISED library contain fluxes at 1221 wavelengths from 9.1 nm to $160 \mu\text{m}$, comfortably covering the entire range where galaxy radiation from stars is significant.

After choosing the viewing direction and the size (up to 160×160 pixels) and resolution for the "virtual CCD camera", the stellar particles are grouped into pixels. For each stellar particle, the spectrum is (flux point by flux point) interpolated from the ISED library. For metallicities lower than the range covered by the library (some stellar parti-

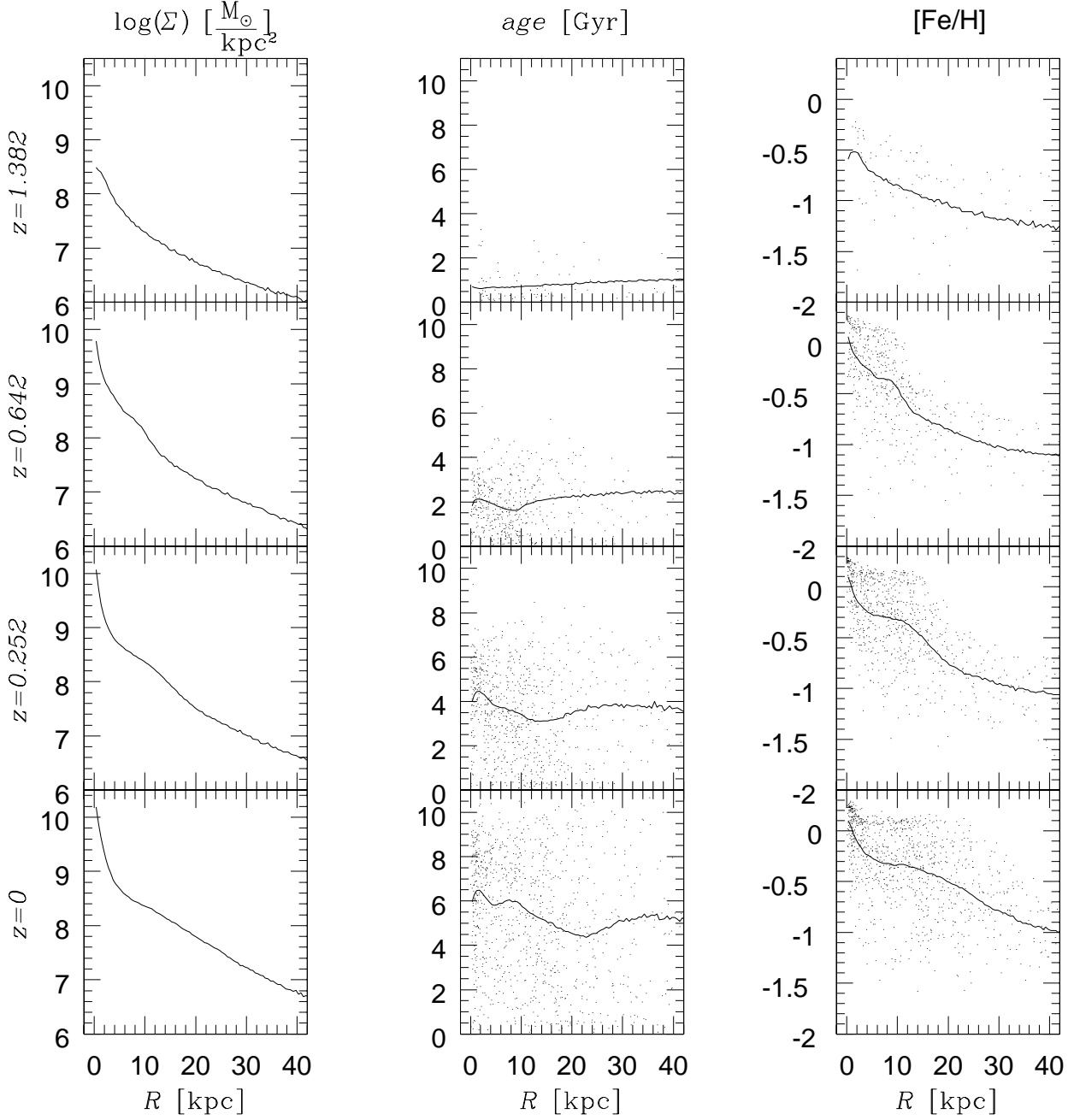


Fig. 3. Surface density profiles (left), stellar particle age (middle) and $[\text{Fe}/\text{H}]$ distribution (right) of the accretion model at four different redshifts (from top to bottom: $z = 1.382$, 0.642 , 0.252 and 0.000 , corresponding to universe ages of 4.5, 7.5, 10.5 and 13.5 Gyr). The lines represent the mean profiles, and the dots show a representative sample of stellar particles.

cles have metallicities down to $[\text{Fe}/\text{H}] = -4.0$, but none have metallicities above the library range), the spectra for the lowest metallicity ($[\text{Fe}/\text{H}] = -2.252$) were used. This should not pose any problems, as trends of spectral properties with metallicity are expected to become weak below $[\text{Fe}/\text{H}] = -2.0$, and these lowest-metallicity stellar particles become negligible in number very soon (~ 0.5 Gyr after the beginning of the simulation).

The spectrum is reddened as follows. According to Quillen & Yukita (2001) we assume a dust-to-gas ratio which is proportional to the metallicity of the gas. The absorption coefficient A_V can be expressed as

$$A_V = \frac{\text{pc}^2}{15 M_{\odot}} \int_{\text{line of sight}} \rho_Z(r) dr \quad (1)$$

with the metallicity-weighted gas density $\rho_Z(r) = \rho_{\text{gas}}(r)Z(r)/Z_{\odot}$. Only the cold cloud medium is assumed

to contain dust. For each stellar particle, $\rho z(r)$ is integrated along the line of sight to derive the absorption coefficient A_V . The spectrum of the stellar particle is then reddened using the extinction law of Fluks et al. (1994).

All the spectra of stellar particles from the same pixel are added up to give the integrated absolute spectrum of the pixel, which is then redshifted and dimmed according to the distance modulus $m - M$ (Carroll et al., 1992).

$$(m - M) = 25 + 5 \log \left(\frac{c(1+z)}{H_0} \right) + 5 \log \left(\int_0^z \frac{dz'}{\sqrt{(1+z')^2(1+\Omega_M z') - z'(2+z')\Omega_\Lambda}} \right). \quad (2)$$

In a next step, we correct the spectra for Lyman line blanketing and Lyman continuum absorption using the formulae given by Madau (1995) for QSO absorption systems. Finally, apparent *UBVRIJHKLM* colours and magnitudes are calculated for each pixel through synthetic photometry. At the same time, the absolute (rest frame) spectra and the apparent spectra of all the pixels are added up to derive the absolute and apparent integrated spectra of the galaxy. An example of such an integrated spectrum is shown in Fig. 4. It shows the intrinsic (upper panel) and the apparent (lower panel) spectra of the accretion model galaxy at $z = 1.065$ from 0 nm to 5000 nm. These spectra differ from previous model spectra, because they take into account the three-dimensional metallicity and age distribution of the stars and the intrinsic dust absorption. However, as one can see from these spectra, gas emission lines are not implemented. Including HII regions, as well as planetary nebulae and supernovae, will be one of the next steps in improving the programme.

On these integrated spectra, synthetic photometry is performed too. At the moment, the spectra of individual pixels or stellar particles are not stored. The final output quantities of the programme are:

1. 2-dimensional *UBVRIJHKLM* images of the model galaxy including the effect of internal absorption in apparent (redshifted and corrected for the distance modulus and Lyman line blanketing and by continuum absorption) magnitudes of up to 160×160 pixels, as seen from a freely chosen angle.
2. the integrated intrinsic spectrum of the entire galaxy plus integrated intrinsic colours and absolute magnitudes.
3. the integrated apparent spectrum of the entire galaxy plus integrated redshifted colours and apparent magnitudes.

We also included the possibility to account for Galactic foreground reddening, but this option only makes sense for specific applications, where the foreground reddening is known. In this work, it is not used.

All these quantities were calculated for both the accretion and the collapse model, at universe ages from 1.5 Gyr (0.3 Gyr after the beginning of the simulations)

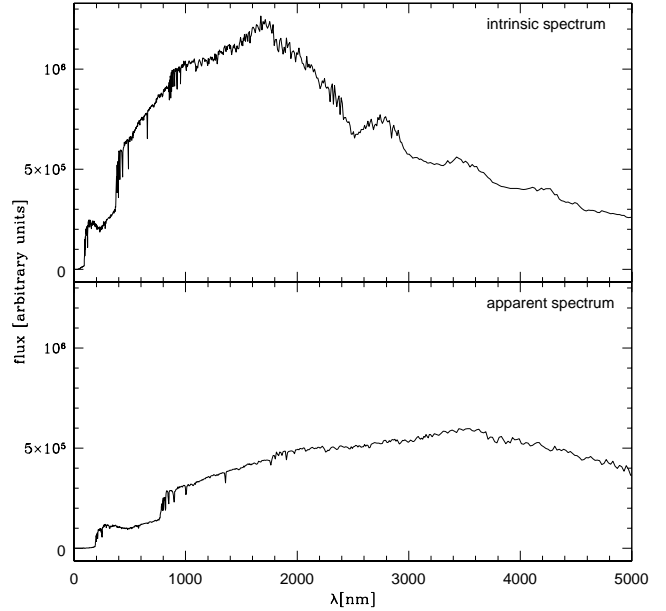


Fig. 4. Intrinsic and apparent (redshifted) spectra of the accretion model at $z = 1.065$ (corresponding to a universe age of 5.5 Gyr).

to 13.5 Gyr (the present day) in steps of 0.5 Gyr, and from three different directions: face-on, inclined by 60° , and edge-on. The size of a pixel was chosen to be 0.5 kpc. At the moment higher resolution makes no sense, as the galaxy model has a resolution of only 0.37 kpc. The entire "camera" was chosen 160×160 pixels wide, thus representing a field of view 80×80 kpc wide.

To study metallicity effects, the face-on and inclined images and spectra were calculated for the accretion model again, but assigning solar metallicity to each stellar particle. The differences between the regular accretion model and this model should therefore purely reflect metallicity effects, allowing us to estimate the error that is made in models using solar metallicity. For the sake of simplicity, we will from now on call this the solar metallicity model.

Analogously, to identify absorption effects, the same photometric properties were calculated for the accretion model without internal absorption. Thus, the differences between the regular model and this one should reflect absorption effects, or the error that is made in models that do not include internal absorption. This model will be called the absorptionless model.

Our synthetic photometric data have been produced in the Johnson-Cousins *UBVRIJHKLM* system, but of course, they can in principle be produced in any system with known passband response functions. Other spectral features, such as line strength indices from the integrated pixel/galaxy spectra can also be derived.

4. Results

A sample of the synthesized U , V , and K -band face-on and edge-on images are plotted in Figs. 5, 6, and 7. Each figure shows the evolution in one colour band (U , V , and K) of the collapse and the accretion models. They show a time sequence starting at 2.5 Gyr with the last image representing the galaxy at the present epoch (ages: 2.5, 3.5, 5.5, 8.5, and 13.5 Gyr, corresponding to $z = 2.57, 1.84, 1.07, 0.49$, and 0.00). The galaxies are appropriately redshifted, but placed at the same distance (something that of course cannot be observed, but is necessary to plot all diagrams with the same scaling), so one sees in these images the effect of the K-correction (the dimming due to redshift and time dilatation), but not the dimming due to the increasing distance modulus. For each colour, all images are scaled in the same way, such that the brightness range spreads 5^m with the brightest pixel of the whole sample overexposed by 3^m (i.e. the brightest 3^m are plotted in white). Already from these images, one can observe interesting evolutionary features. The collapse model shows its most interesting features at the beginning of its evolution, when its SF is strongest. At a universe time of 3.5 Gyr, when the core is already burnt out, a ring-shaped star forming region appears, and collapses at 4.5 Gyr to a bar and two spiral arms. The bar survives until around 10.5 Gyr, and from there on the galaxy appears as an early disk-type galaxy until the present day.

The fact that in the U and V band figures, the $z = 0$ images are the brightest, whereas these magnitudes are expected to peak at $z \simeq 1 - 2$, when the SFR peaks, is due to the K corrections (see the middle row of panels in Fig. 8), and is not seen in the evolution of the intrinsic integrated magnitudes M_U and M_V (Fig. 8, top row). In the K band, the K correction (Fig. 8, middle right panel) is much smaller than in the visual and ultraviolet, which makes the well-known property of the K magnitude as a (stellar) mass tracer hold approximately true even at high redshift. Therefore, the brightness of these images levels off at $z \simeq 1$, when the bulk of the SF is completed. The accretion model shows its most prominent features at low redshift. Among them are a bar, formed at ~ 6 Gyr and spiral arms, formed a bit later. Both features survive until the present epoch.

4.1. Integrated photometric quantities

In tables A.1 to A.10, the integrated photometric properties (rest frame absolute colours and magnitudes, K corrections, and apparent colours and magnitudes according to the used cosmology) are summarized for both models in the inclined view (60°). The integrated (intrinsic and apparent) magnitudes of the inclined view lie somewhere between the ones of the face-on and of the edge-on view, but closer to the magnitudes of the galaxy seen face-on. In the accretion model, the inclination does not play a role for the intrinsic apparent magnitudes until a redshift of ~ 1.4 , because only then, the disk begins to form. From

then on, the face-on view becomes gradually brighter than the edge-on view in all passbands. At $z = 0$ the difference amounts to $\sim 0.6^m$ in m_U , m_B , m_V , m_R and m_I and $\sim 0.15^m$ in m_K . The spatial resolution of the simulations is still too low, to resolve the vertical stratification of the gaseous disk. Therefore, the absorption in the edge-on view is overestimated and the differences between face-on and edge-on view are only upper limits.

The same is seen for the collapse model, but much earlier and with a higher magnitude. The two models diverge already at a redshift of ~ 2 and reach differences of $\sim 1^m$ (m_U , m_B , m_V , m_R , m_I) resp. $\sim 0.5^m$ (m_K).

Integrated photometric properties (in the inclined view) are shown as a function of redshift in Figs. 8 to 10. In the absolute magnitude diagrams (Fig. 8, top row), we see again that the brightening of the accretion model begins to level off at $z \sim 1$, while the collapse model has already passed its zenith. The absolute magnitude evolution is shown here only for M_U , M_V , and M_K , but it looks similar in all bands.

The K corrections are shown in the middle row of Fig. 8. The strong K_U correction for $z > 3$ is caused by the Lyman line blanketing and Lyman continuum absorption. The K_B looks similar to K_U ; the same holds for (K_V , K_R and K_I), and for (K_K , K_J , K_H , and K_L).

In the m_U , and m_V diagrams of Fig. 8, bottom row (here again, the same diagrams for m_B , m_R , m_I , m_J , m_H , and m_L would look very similar), the approximate HDF limiting magnitudes of the $F300W$, $F606W$ and $F222M$ bands for the Hubble Deep Field North (Williams et al., 2000) are shown as dotted lines. These limits indicate that we should see galaxies like the one modelled in the accretion model out to a redshift of 2.4 in the visible and infrared passbands according to the J_{110} and H_{160} limits of the NICMOS HDF counterpart (Thompson et al., 1999). The HDF objects seen at higher redshift are probably the progenitors of more massive early type galaxies (E or S0), rather than young disk galaxies. Morphologically, they may be hard to distinguish at these redshifts, as the model galaxies do not show their disk structure yet. This is confirmed at least qualitatively by Abraham et al. (1999a,b). The collapse model should be seen in the HDF out till $z \simeq 3$ in m_U or even ~ 3.5 in m_V , m_I , m_J or m_H . The HDF limits also indicate that we need to go $\sim 4^m$ fainter in V and I , $\sim 10^m$ in U to catch a galaxies like the accretion model near birth.

The intrinsic colours (Fig. 9) become redder with time for both models, with the collapse model colours starting off bluer than the accretion model colours, but becoming redder than the latter at $z \simeq 3$ in all colours, which is not surprising, if we take the star formation history into account.

The oscillating evolution of the apparent colours (Fig. 10) is a combination of the evolution of the corresponding intrinsic colour and the K corrections (see Fig. 8) of the two involved passbands. Again, the collapse model starts off bluer in all colours and turns redder than the accretion model at $z \simeq 3$. Interestingly though the collapse

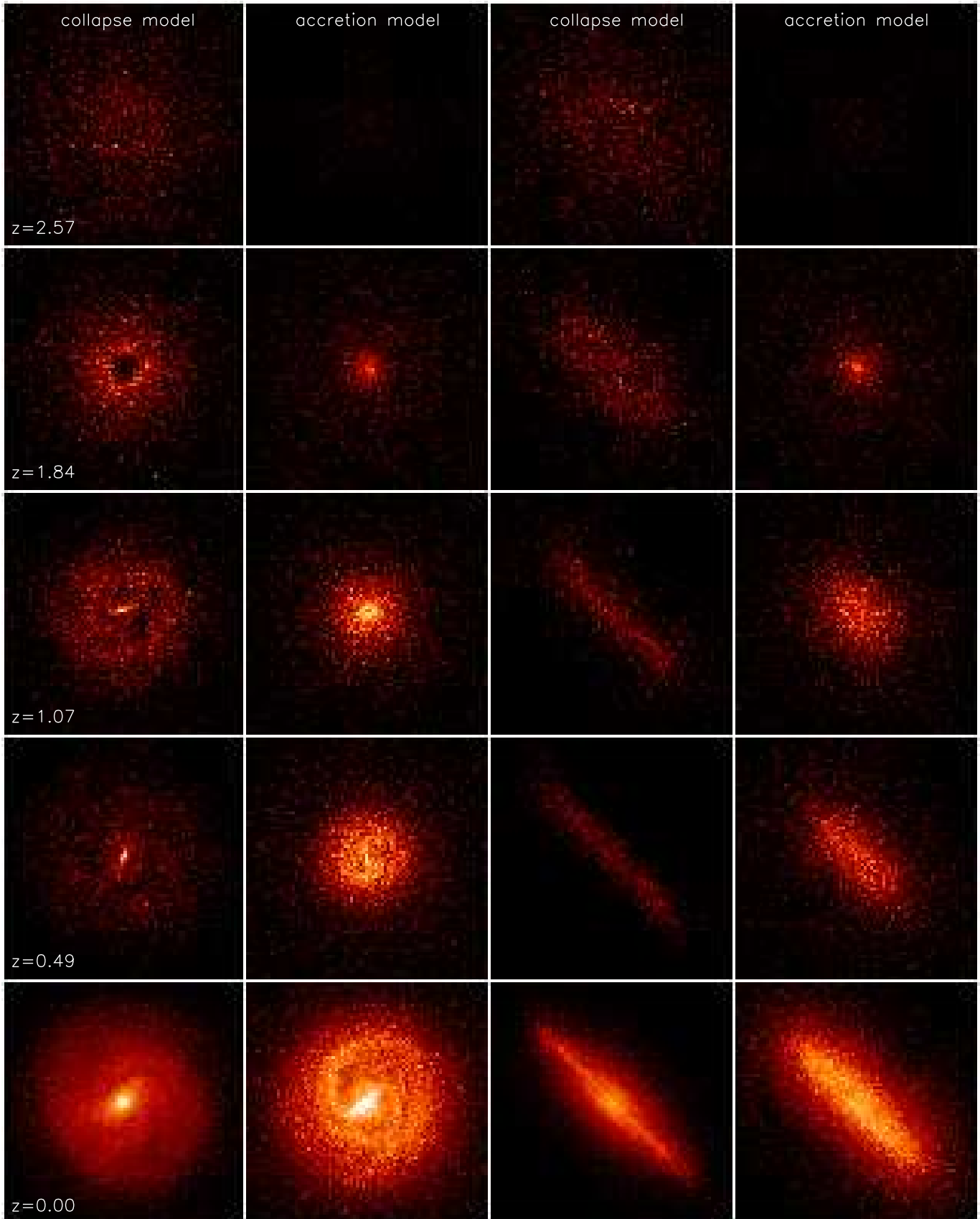


Fig. 5. U band evolution of the collapse and the accretion models. First column: collapse model, face-on, second column: accretion model, face-on, third column: collapse model, edge-on, fourth column: accretion model, edge-on. The wavelength ranges that are shifted into the U band here correspond to "bands" with effective wavelengths (from top to bottom) 103 nm, 129 nm, 177 nm, 246 nm, and 367 nm (U band).

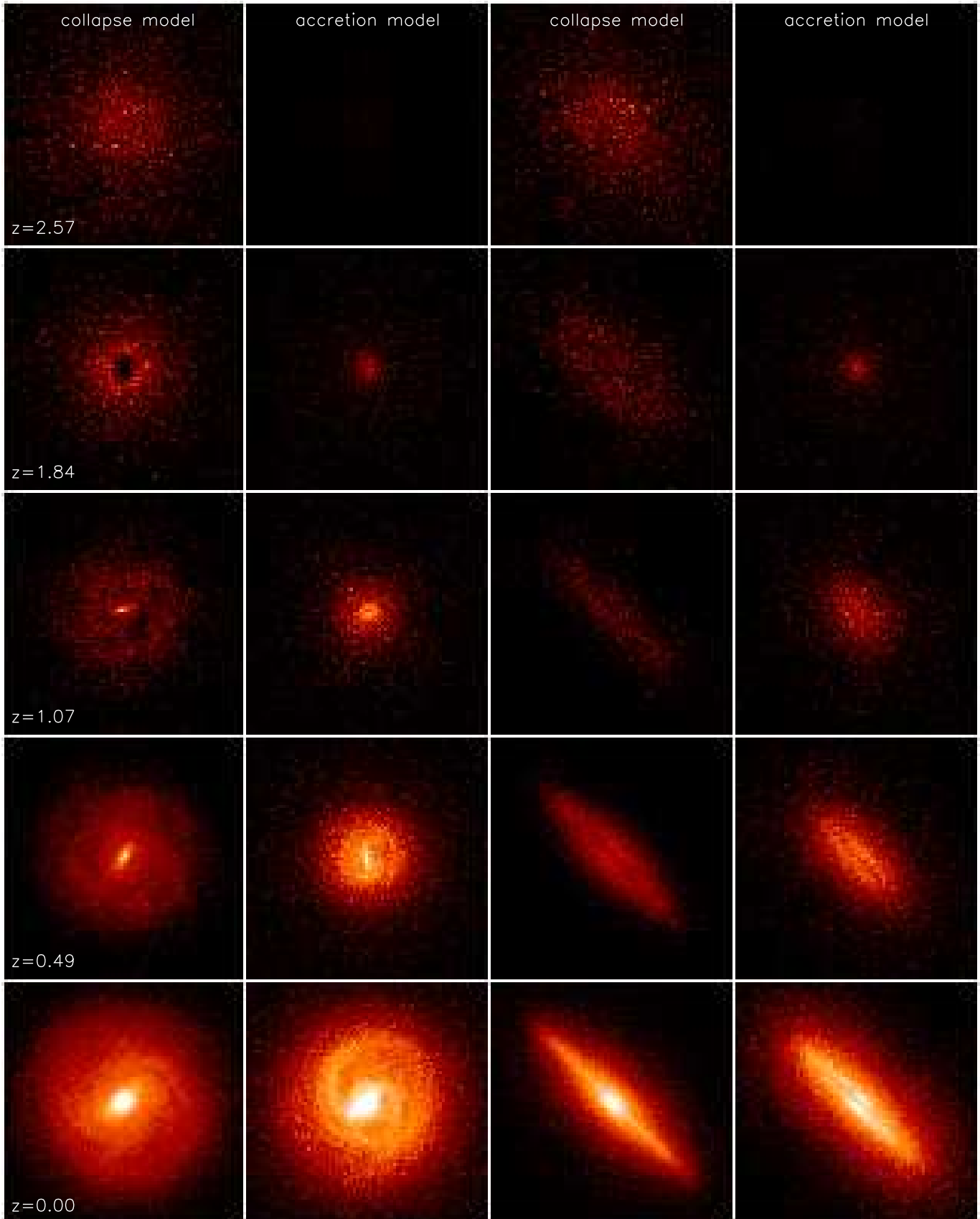


Fig. 6. V band evolution of the collapse and the accretion models. First column: collapse model, face-on, second column: accretion model, face-on, third column: collapse model, edge-on, fourth column: accretion model, edge-on. The wavelength ranges that are shifted into the V band here correspond to "bands" with effective wavelengths (from top to bottom) 153 nm, 192 nm, 263 nm, 366 nm ($\sim U$) and 545 nm (V band).

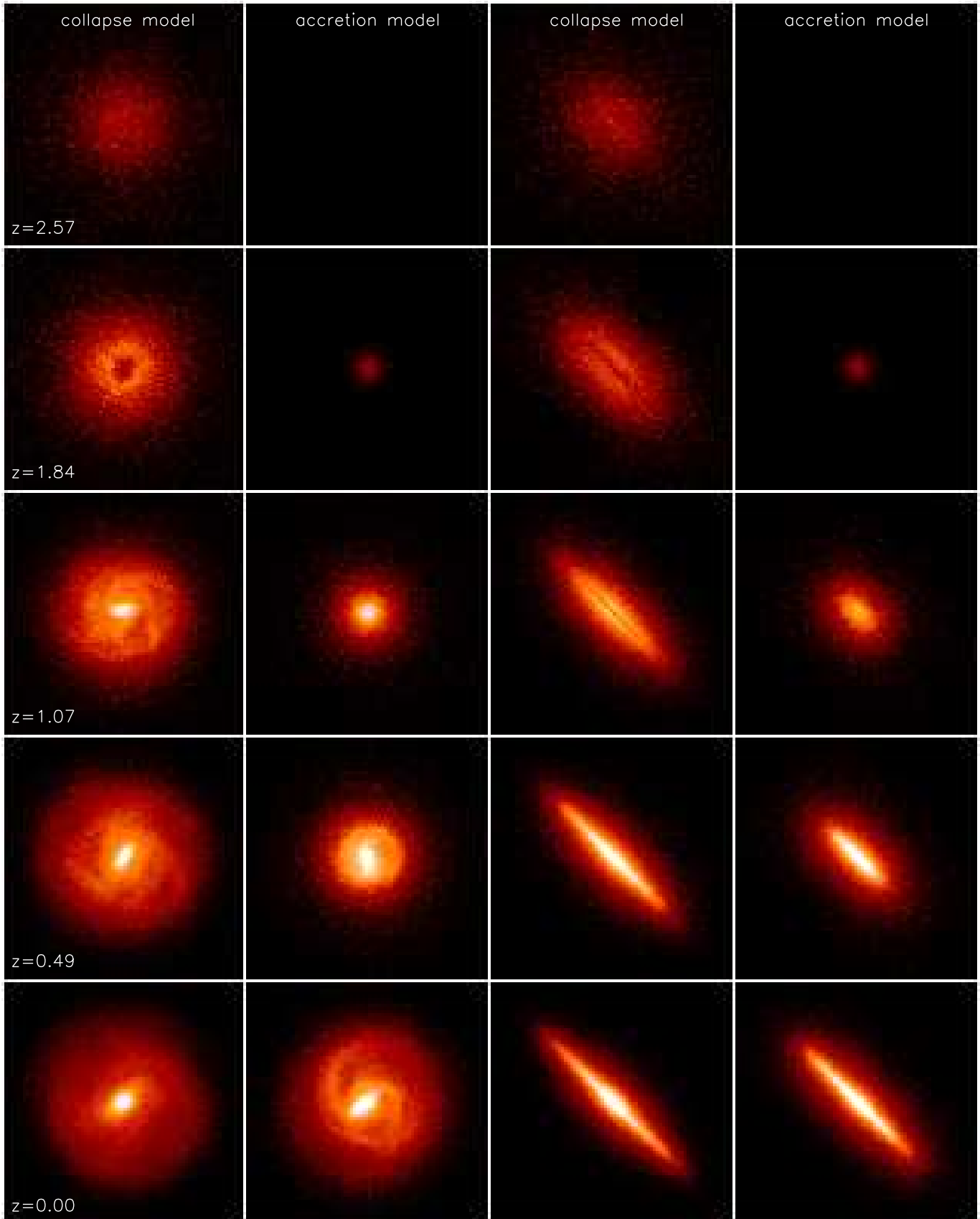


Fig. 7. K band evolution of the collapse and the accretion models. First column: collapse model, face-on, second column: accretion model, face-on, third column: collapse model, edge-on, fourth column: accretion model, edge-on. The wavelength ranges that are shifted into the K band here correspond to "bands" with effective wavelengths (from top to bottom) 613 nm (between V and R), 771 nm ($\sim I$), 1060 nm (between I and J), 1470 nm (between J and H), and 2190 nm (K band).

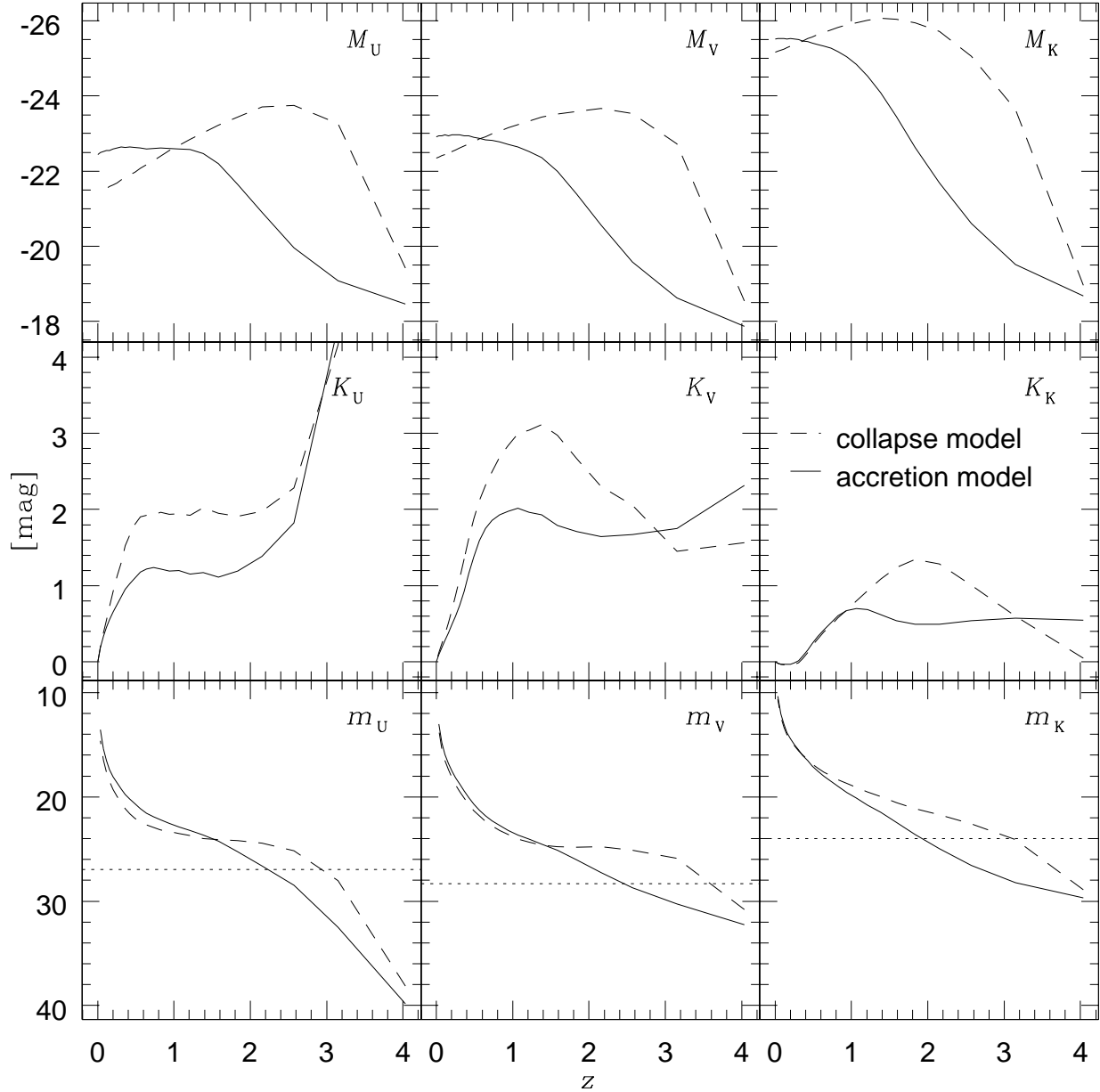


Fig. 8. Evolution of integrated photometric properties (from top to bottom: absolute magnitudes, K corrections and apparent magnitudes) of the accretion model (solid) vs. the collapse model (dashed) as a function of redshift in three passbands (from left to right: U , V , and K) and at inclination 60° . The dotted lines in the apparent magnitude diagrams represent the approximate limiting magnitudes in the $F300W$, $F606W$ and $F222M$ bands for the Hubble Deep Field North (Williams et al., 2000). The conversion from evolution time to redshift assumes a standard Λ CDM cosmology.

model does not show the very red colours at intermediate redshift that are predicted (Zepf, 1997; Barger et al., 1999) by monolithic models like those of Arimoto & Yoshii (1987) or Matteucci & Tornambe (1987). Zepf (1997) predicts, for example, $V - K$ colours of up to ~ 7 , whereas our collapse model does reach only $V - K = 5$, due to the modest, but in the integrated light important SF that

continues until the present epoch (Fig. 2). This shows that the lack of observed red galaxies does not exclude the possibility that some galaxies formed early in a single collapse out of one protogalactic gas cloud, provided that a minimum SF is maintained after the main "starburst".

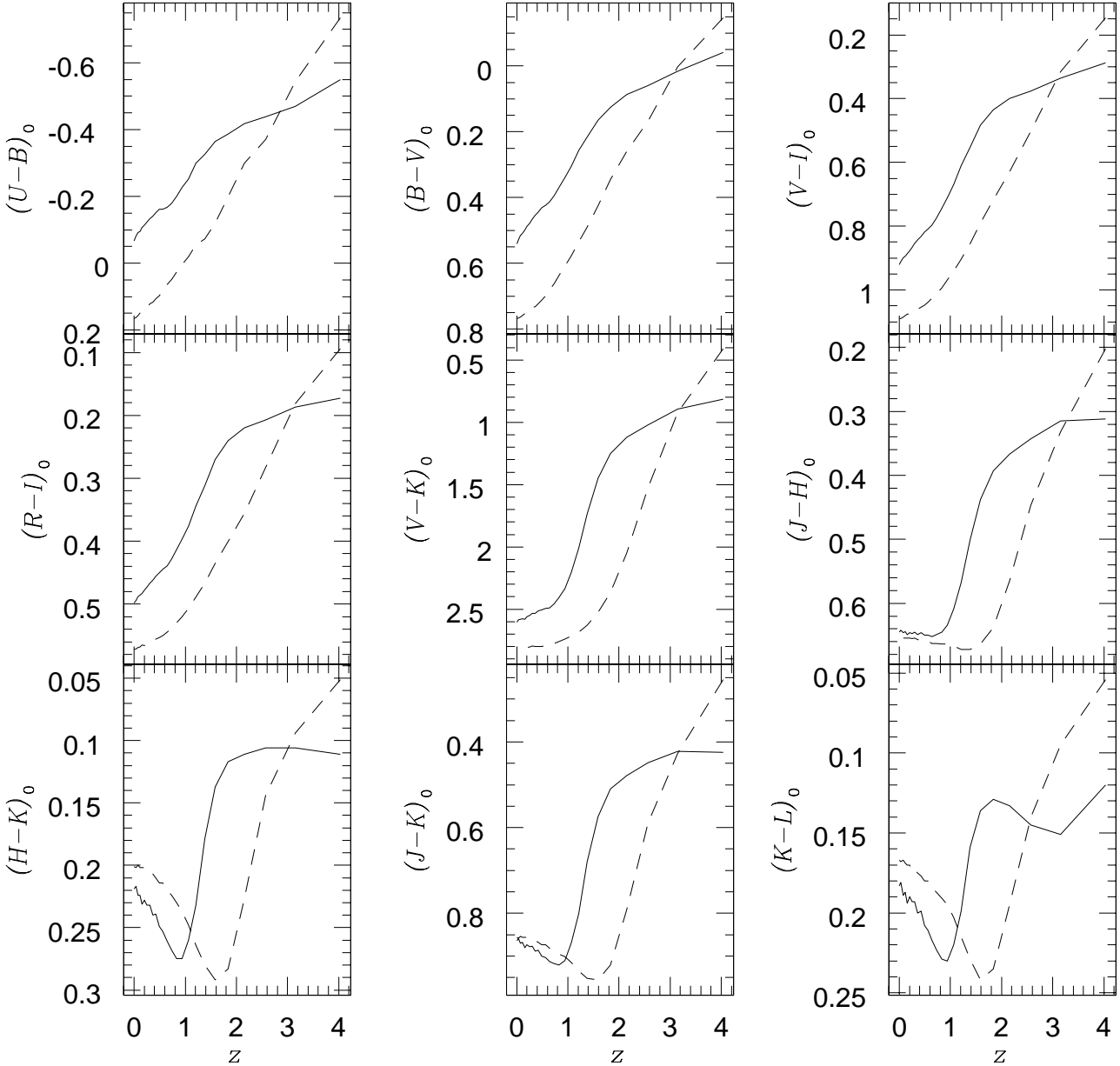


Fig. 9. *UBVR IJHKL* intrinsic integrated colour evolution of the accretion (solid) and the collapse model (dashed) as a function of redshift and at inclination 60° .

4.2. Interpretation of the integrated photometric quantities

In the following, we concentrate on the accretion model. In order to interpret the evolution of the intrinsic colours (table A.1 and A.2), we compare them with the colour evolution of SSPs (Fig. 11). These were also produced with the GISSEL code, using the same tracks, stellar library and IMF as for the galaxy model, so any systematics stemming from the input SSP spectra should cancel out (actually these are the SSPs, from which the model galaxy

colours were derived). The two SSPs shown here are for solar metallicity (dash-dotted), which is not far above the average metallicity at which the galaxy model ends, and $[\text{Fe}/\text{H}] = -2.252$ (long dashes), the lowest metallicity available. The regions between these two curves are shaded to show the ranges in which the colours of SSPs evolve. The solid lines represent the colour evolution of the accretion model. In order to identify metallicity and absorption effects, the solar metallicity and the absorptionless models (see Section 3) are shown as dashed resp. dotted lines.

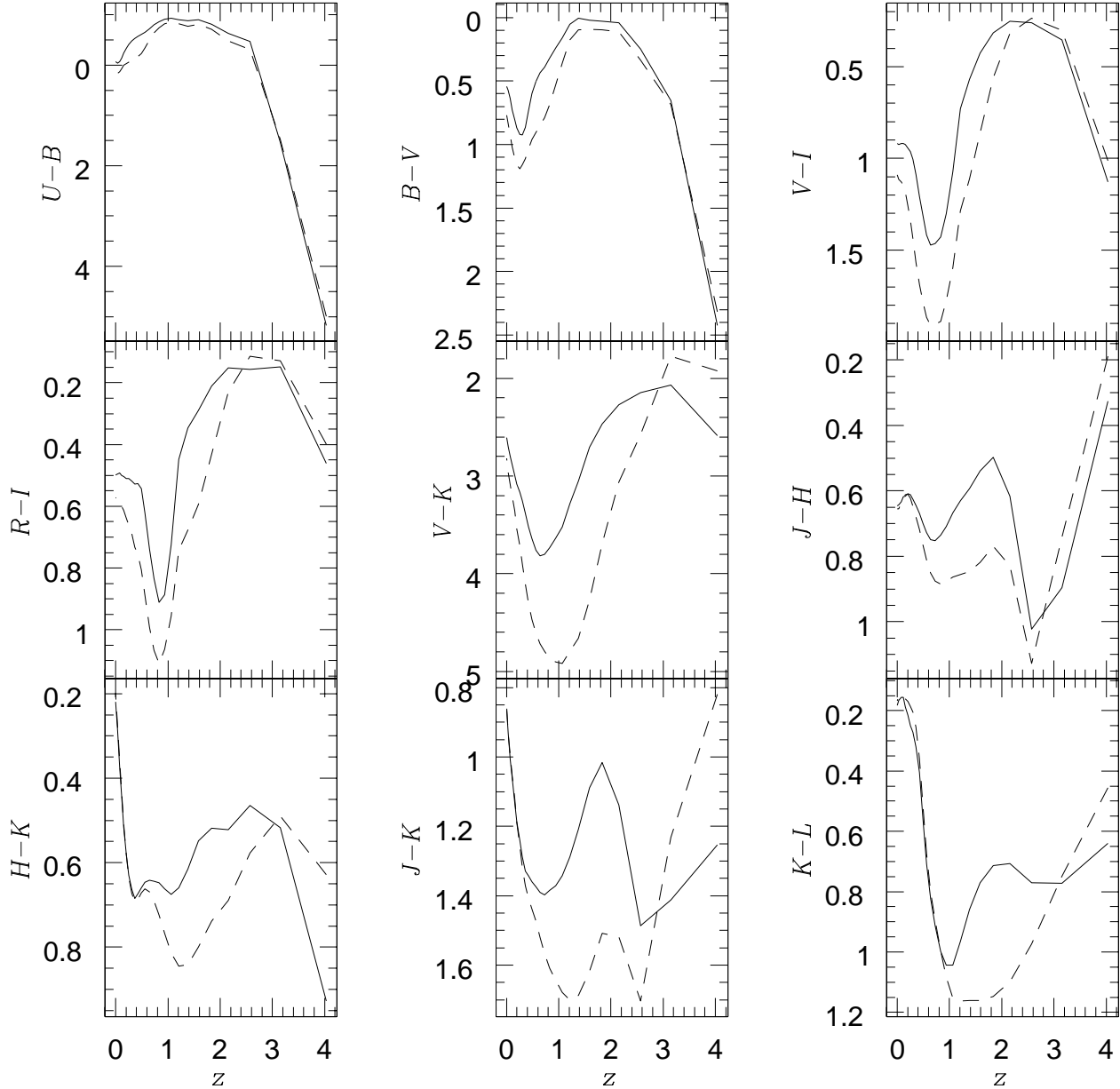


Fig. 10. Predicted $UBVR IJHKL$ observed integrated colour evolution of the accretion (solid) and the collapse model (dashed) as a function of redshift and at inclination 60° .

Of course all three, the accretion model, the solar metallicity model, and the absorptionless models behave smoother with redshift than the SSPs, because they represent convolutions of SSPs with an SFR. In $(U - B)_0$ (the metallicity indicator for individual stars), $(V - I)_0$, and other ultraviolet and optical colours not shown here, ongoing star formation dominates the colours, so the models remain even bluer than for the $[\text{Fe}/\text{H}] = -2.252$ SSP during the entire evolution. The SF determines the colour evolution as long as SF continues and metallicity and absorption change these two colours by less than 0.1^m . It is

expected that the colours will rapidly (within a few Gyr) tend towards the lower (solar metallicity) curve once SF is completed. In the infrared colours $(V - K)_0$ and $(J - K)_0$, where SF does not leave such a strong imprint, we see a combination of SF and internal reddening, placing the colours well below the $[\text{Fe}/\text{H}] = -2.252$ SSP evolution from $z \simeq 1.4$ on. $(J - K)_0$ comes out even redder than the solar metallicity SSP for a few Gyr around $z = 1$, when the gas density in the centre of the model galaxy is the highest. The fact that the absorptionless model (dotted) lies between the two SSPs proves that this is an absorp-

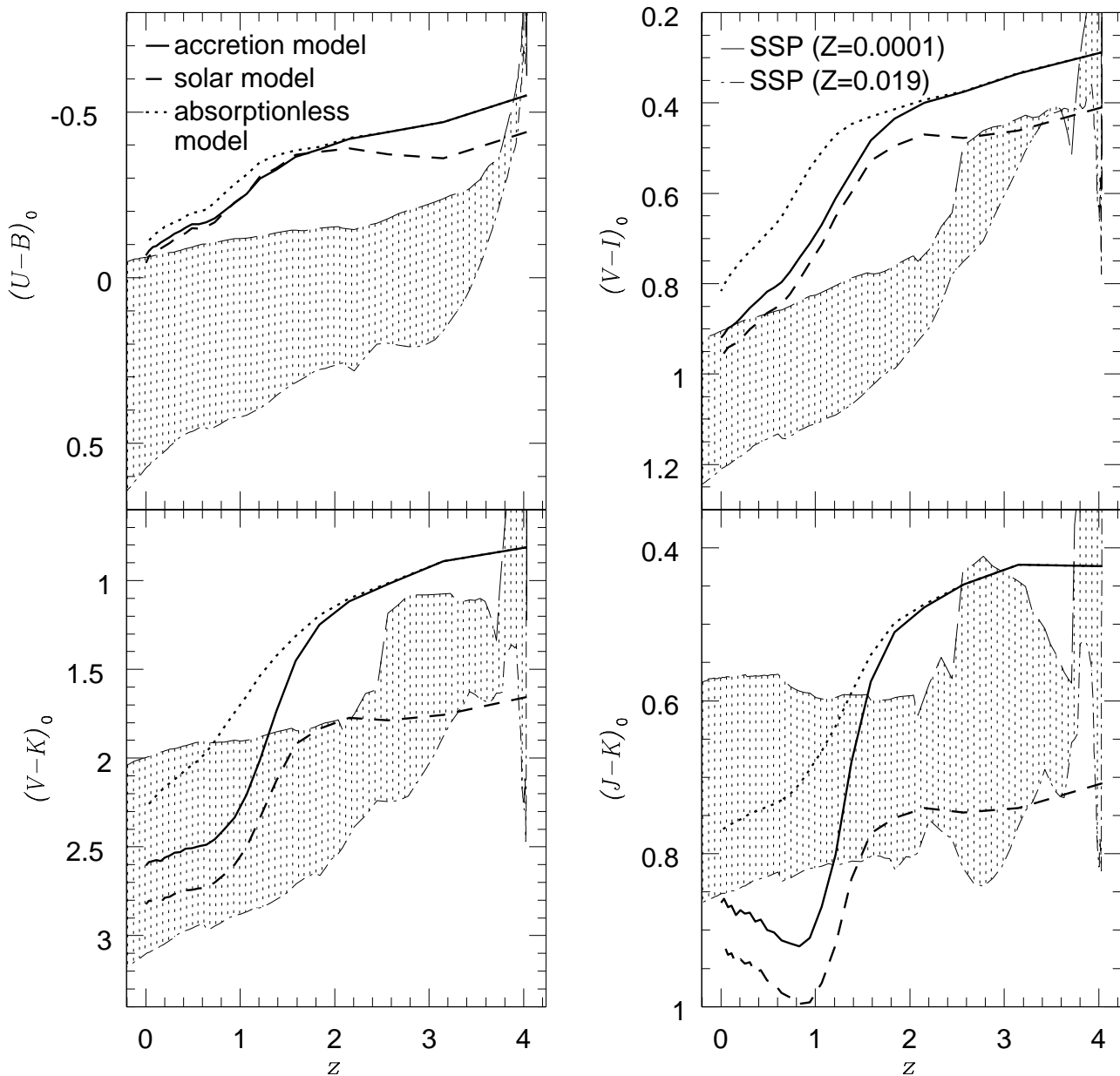


Fig. 11. Integrated intrinsic colour evolution in four colours ($U - B$, $B - V$, $V - K$, and $J - K$) as function of redshift for the accretion model (solid), compared to the evolution of single stellar populations, born at $z = 4$, with two different metallicities (dash-dotted: solar, long dashed: $[\text{Fe}/\text{H}] = -2.25$, the region between these two curves is shaded). In dashes, the colours are shown for the solar metallicity model, and in dotted lines for the absorptionless model.

tion effect. These colours are of course also expected to tend towards the ones of the solar SSP with time. As can be seen from the colour evolution of the solar metallicity model (dashed), the metallicity effect is relatively minor for $z \lesssim 1.4$. With $\simeq 0.2^m$ in $(V - K)_0$ and $\simeq 0.1^m$ in $(J - K)_0$, it is stronger than in the ultraviolet and optical colours, even though these infrared colours are known to be metallicity insensitive for individual stars.

Obviously, different rules apply for the metallicity dependence of colours for composite stellar populations than for individual stars. This is explained by the fact that, by comparing populations of different metallicities, we are not looking at stars of the same stellar parameters, but at stars of the same age. Populations of the same age do not necessarily show the same metallicity dependence as stars of the same stellar parameters (that is, a strong

metallicity dependence in the ultraviolet and metallicity independence in the infrared). As stars of different $[\text{Fe}/\text{H}]$ develop differently (metal-rich stars have longer lifetimes than metal-poor stars of the same mass), the infrared colours do depend on metallicity for stellar populations. This can actually already be seen from the colour evolutions of SSPs in Fig. 11. Hence, in our galaxy model, metallicity effects can be observed in $(J - K)_0$, whereas in $(U - B)_0$, they are suppressed as long as SF continues.

So far, we have discussed only intrinsic colours. For the comparison with real galaxies, we have to look at the evolution of the redshifted intrinsic colours. This evolution is shown in Fig. 12 for the same colours as in Fig. 11 (the comparison with SSPs is omitted here). Again, $U - B$ is only slightly affected by both metallicity and absorption, and mainly reflects SF and the absorption of intervening gas at high redshifts. In $V - I$, the differences between the accretion model and the solar metallicity model amount to 0.2^m at high redshift, but become negligible at $z \simeq 2$. From then on, absorption effects become important, but they do not change $V - I$ by more than 0.15^m . Metallicity is crucial for the evolution of the infrared colours $V - K$ and $J - K$. At high redshift, it can change $V - K$ by up to 0.75^m , and $J - K$ by 0.25^m . At $z = 0$, the difference is still 0.2^m resp. 0.05^m .

Absorption is most important at $z \lesssim 2$. At $z \simeq 1$, it changes $V - K$ by 0.6^m , and $J - K$ by 0.25^m . The main difference between the evolution of the two infrared colours shown here is seen from $z \simeq 1.8$ to $z \simeq 2.6$, when $J - K$ becomes bluer by $\sim 0.4^m$, due to the 4000 \AA break that wanders through the J band between these redshifts.

The lack of absorption effects in all colours at high redshift in these models is explained by the lack of gas in the dark halo at this epoch. Of course, the gas that falls in at a later stage is already there outside the halo, and its absorption would in principle have to be included in our models too, but it is distributed over such a large volume that only a negligible fraction will be located in the line of sight.

From the large metallicity and absorption influences on colours, it follows that the metallicity distribution of the stars and the internal absorption by gas must be taken into account when deriving colours from galaxy models.

4.3. Bulge colours

To test the properties of our models, we compared the colours of HDF-N disk galaxy bulges from Ellis et al. (2001) with our results. We expect bulge colours to be more accurate than integrated galaxy colours, as they are usually measured within isophotes well above the noise level. To derive bulge colours from our models, we located for each "frame" the highest concentration of light, and calculated the integrated colours over a range of 1.25 kpc around this centre (corresponding to around 20 "pixels"). Varying this "aperture size" showed that this is a reasonable value. It also corresponds well to the aperture used

by Ellis et al. (2001). Tables B.1 and B.2 summarize our bulge colours for the face-on and the edge-on view, and in Figs. 13 and 14, the redshift evolutions of $V - I$ and $J - H$ are plotted, as well as the empirical data, which had to be transformed from the HST $V_{606} - I_{814}$ resp. $J_{110} - H_{160}$ system into Johnson-Cousins $V - I$ (Fukugita et al., 1995) and $J - H$ (Stephens et al., 2000). The thick points in Figs. 13 and 14 show the transformed data, while the crosses in the $V - I$ diagram are still in the HST system, as no transformation was available. The model predictions for the face-on (dashed), the inclined (solid), and edge-on (dotted) view are drawn as thick lines, and for comparison, the integrated colours of the same models are shown as thin lines. The Ellis et al. (2001) integrated galaxy colours are not shown here in order not to overload the figure. On average, they are only around 0.1^m bluer than their bulge colours, whereas our model predicts them to be 0.2^m to 0.3^m bluer. This is probably due to the fact, that we calculate the model galaxy colours by using all the light out to 40 kpc from the galactic centre. The model shows a colour gradient in the sense that the galaxy is bluer in the outer parts. In fact, the colour of the model galaxy integrated over the inner 10 kpc is less than 0.1^m bluer than the bulge colour. This is why, in our comparison with observations, we use bulge colours rather than full galaxy colours. Clearly, the models reproduce the observed colours well. One can argue that our $J - H$ predictions are too blue, but they are within the measuring errors ($\sim 0.15^m$).

The different evolutions of the edge-on model and the face-on model bring us to an interesting result: At low redshift, the models predict much redder bulge colours for edge-on than for face-on galaxies. The inclined model follows the face-on model more or less. The difference amounts to 0.5^m in both $V - I$ and $J - H$ (the two colours studied here, but the effect is present in all colours). This is due to absorption from the dust in the disk. In $J - H$, this absorption begins to take its toll already at a redshift of 1.2, whereas in $V - I$, it does not appear until $z \simeq 0.4$. This corresponds well with the fact that the V and I band are shifted into the J and H band at redshift ~ 1 . In the edge-on view, the absorption effect is overestimated as a result of the limited spatial resolution in our models. In the models, a significant fraction of the bulge is reddened by the thick gas disk, while in observed galaxies, the absorbing material is concentrated in a thin disk, which affects only a small fraction of the bulge. Nevertheless, this result shows that it is important to know the inclination of disk galaxies, in order to interpret their bulges' colours, especially if one wants to compare the colour evolution of these bulges with the colour evolution of elliptical galaxies.

4.4. Magnitude - and colour profiles

Finally, we study the profiles in different colours and magnitudes and their possible correlations with the profiles of the physical quantities presented in Section 2, Fig. 3, stel-

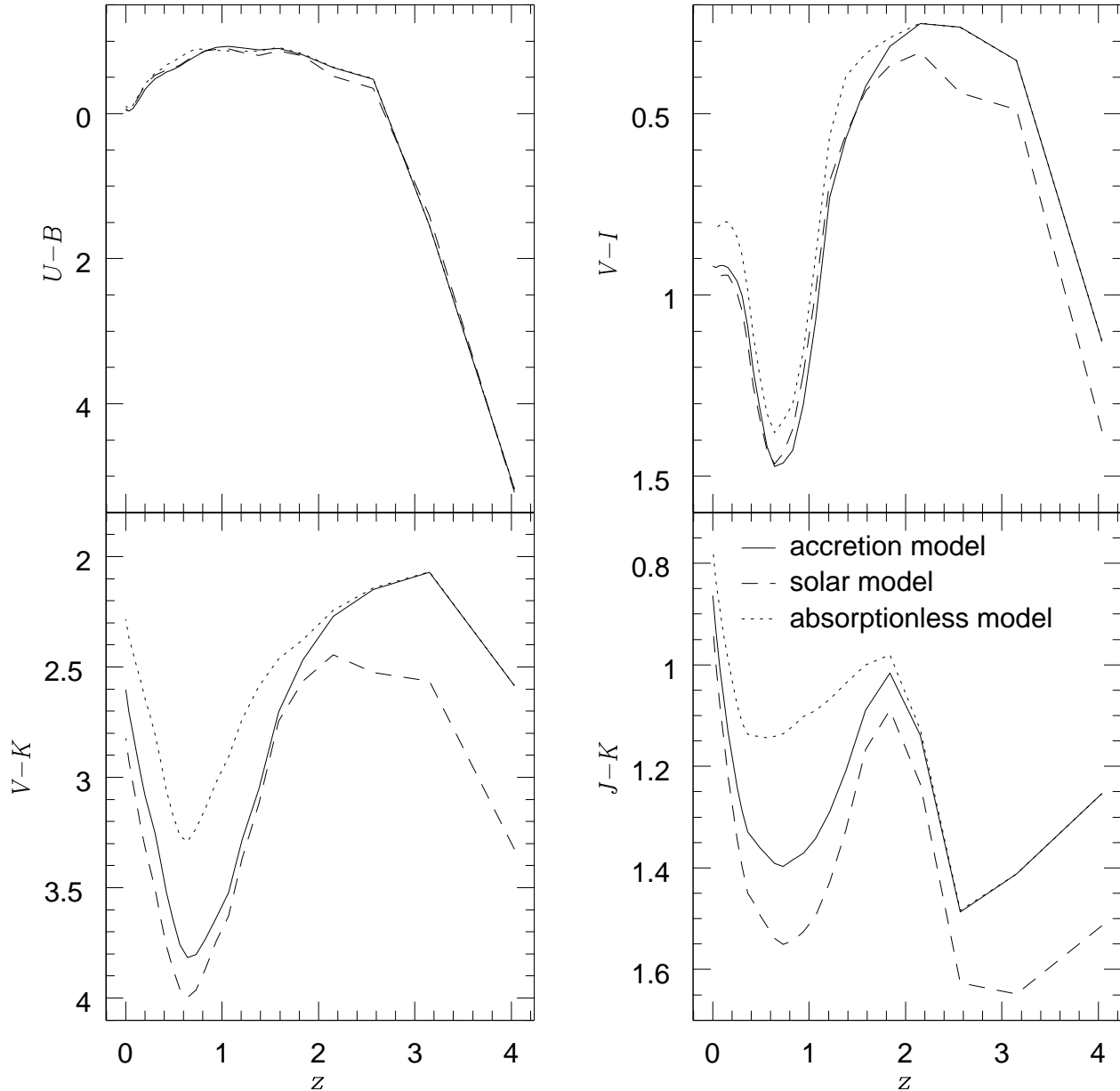


Fig. 12. Integrated observed colour evolution in four colours ($U - B$, $B - V$, $V - K$, and $J - K$), as function of redshift, for the accretion model (solid) compared to the solar metallicity model (dashed), and the absorptionless model (dotted).

lar mass surface density, stellar particle age, and stellar metallicity.

The apparent magnitude profiles (calculated in the same way as for the quantities in Fig. 3) in U , V , and K are shown in Fig. 15 as solid lines. In order to see if there are any metallicity or absorption effects on these profiles, the same profiles are drawn as dashed lines for the solar metallicity model, and as dotted lines for the absorptionless model. All magnitude profile plots are scaled

in the same way which means 1^m has the same size in all plots, so they can directly be compared.

As expected, all three profiles reflect the mass density, whereas the metallicity gradient causes only a small modification, which in real data can hardly be disentangled from the mass density contribution. The best mass density tracer is obviously m_K , which is well known for this property. It follows the mass density perfectly, and shows almost no metallicity or absorption influence. An agreeable property of m_K as a mass tracer is that it holds true

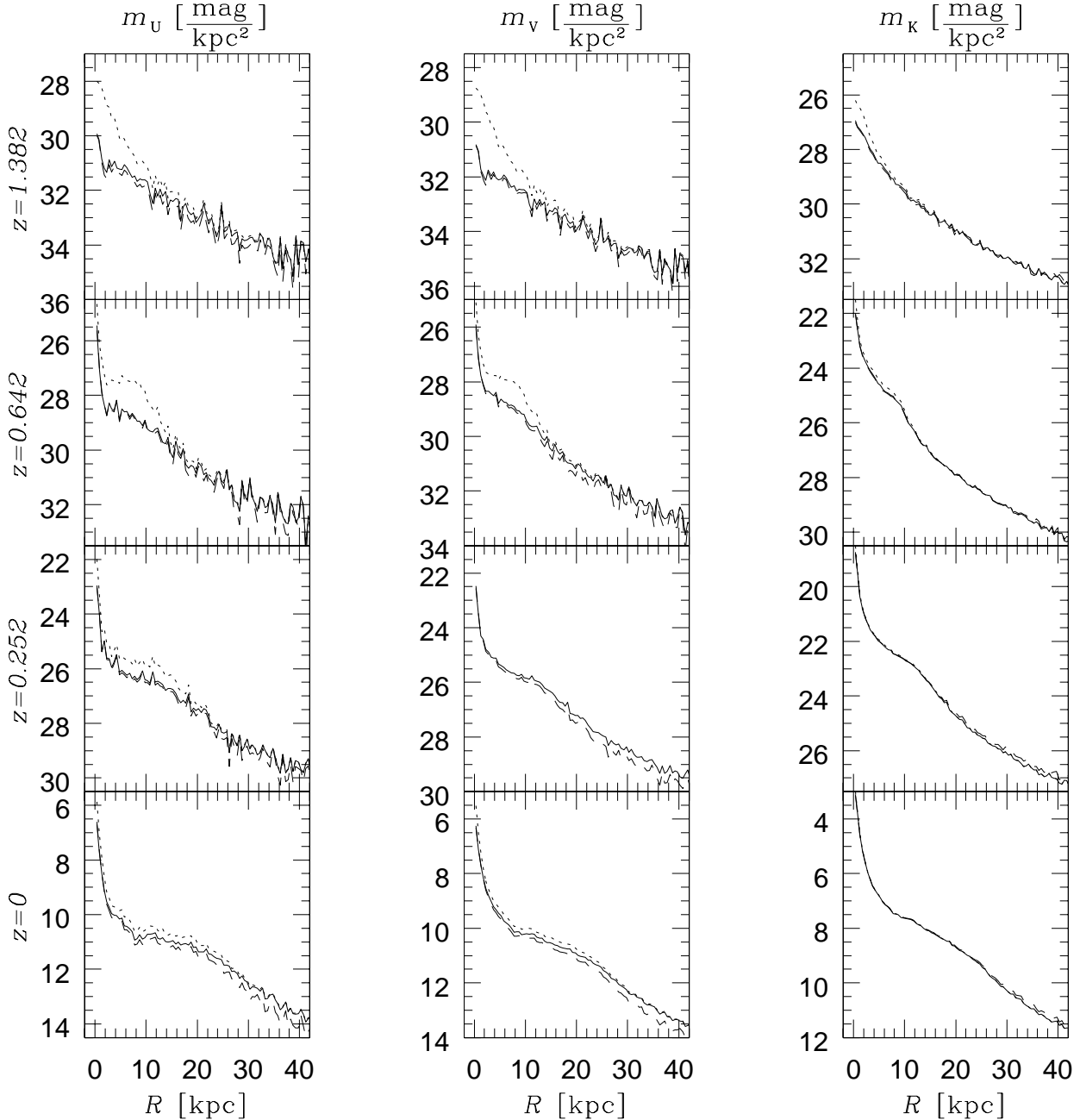


Fig. 15. Apparent magnitude profiles in the U , V , and K (from left to right) passbands for the accretion model (solid), compared with the profiles of the solar metallicity model (dashed) and the absorptionless model (dotted), for the same redshifts as in Fig. 3.

even for the redshifted models, although we are actually looking at wavelength regions corresponding to the I , J , and H bands there. In m_U and m_V , absorption amounts to $\sim 2^m$ in the centre at redshifts around 1.

More surprising are the results for the colour gradients. In Fig. 16, they are shown for $U - B$, $V - I$, and $J - K$ as solid lines vs. the same profiles for the solar metallicity model (dashed) and the absorptionless model (dotted). Again, they are plotted on the same scale for each redshift. Surprisingly, $U - B$ and $V - I$ prove almost

metallicity independent (the $U - B$ profile at $z = 1.382$ should not be over-interpreted, because the stellar library was not calibrated in the range that is shifted into the U and B here), whereas metallicity seems to leave a stronger effect on $J - K$ (at the same time, absorption is negligible here), a result we already encountered for the time evolution of the integrated light of the two models. Indeed, the profiles of the differences $\Delta(J - K)$ between the regular accretion model and the solar metallicity model (shown for low redshifts in Fig. 17) are well correlated with the

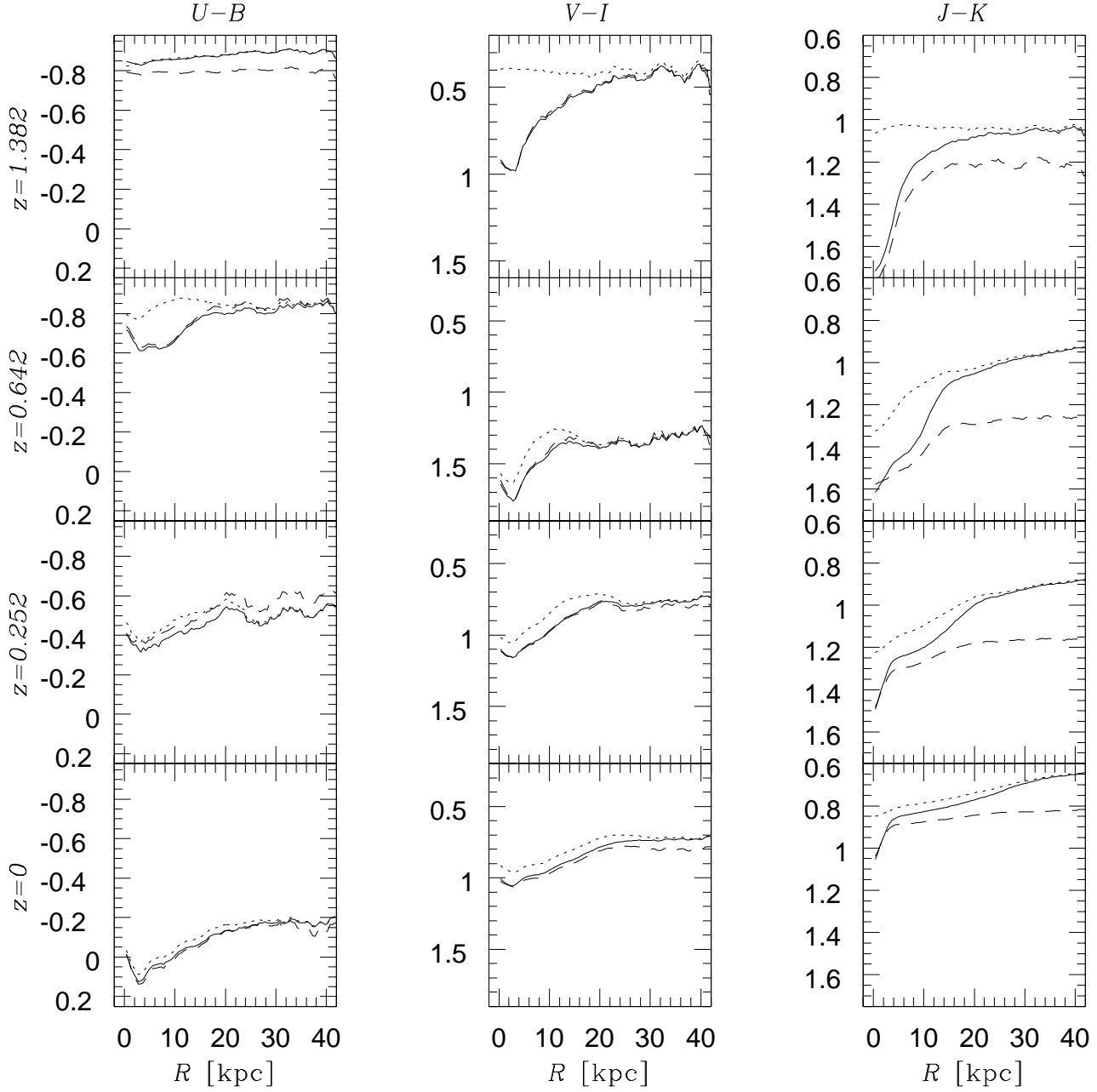


Fig. 16. Colour profiles in $U - B$, $V - I$, and $J - K$ (from left to right) for the accretion model (solid), compared with the solar metallicity model (dashed) and the absorptionless model (dotted), for the same redshifts as in Fig. 3.

[Fe/H] profile (Fig. 3). There is some profit to be taken from this, due to the fact that the solar metallicity model profile is more or less horizontal (apart from the inner bulge; Fig. 16), at least at low redshift. This means that a $J - K$ gradient should be directly related to the metallicity gradient, even though the absolute colour will not necessarily yield the absolute [Fe/H] value. We find

$$\frac{d[\text{Fe}/\text{H}]}{dR} \simeq 4 \cdot \frac{d(J - K)}{dR}, \quad z \leq 0.5. \quad (3)$$

Of course, this finding needs to be confirmed observationally, but it is an indication that $J - K$ could prove a useful metallicity gradient tracer.

5. Discussion and Conclusions

We present the spectral analysis of two chemo-dynamical galaxy formation models, evaluated with a state of the art evolutionary code and spectral library. The programme transforming the models into spectral properties takes into account the three-dimensional distribution of the stars and

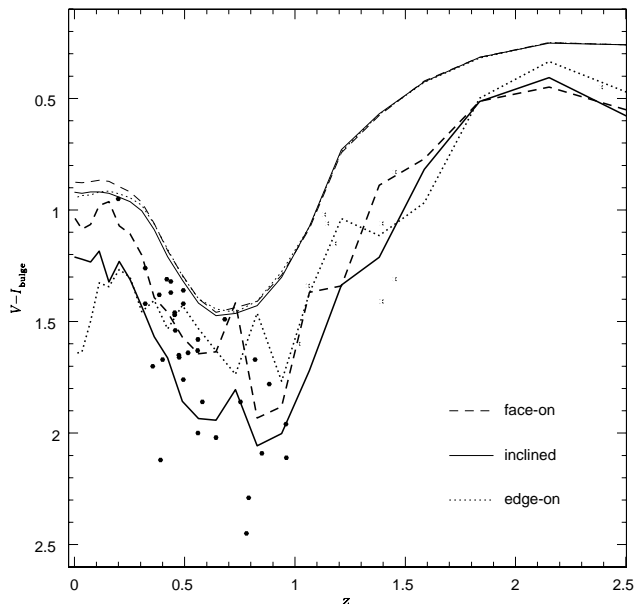


Fig. 13. Predicted bulge $V - I$ colours (thick lines) as function of redshift from the accretion model for three different inclinations (dashed: face-on, solid: inclined by 60° , dotted: edge-on), compared to HDF disk galaxy bulge colours (Ellis et al., 2001), transformed into the standard system according to Fukugita et al. (1995) (thick points). For the crosses ($z > 1$), the colours were kept in the HST $V_{606} - I_{814}$ system, as no transformation equation was available. The integrated model colours for the three inclinations are shown as thin lines.

the interstellar matter. It includes internal gas absorption and is also able to include foreground reddening.

We obtain two-dimensional $UBVR IJHKL M$ images of the model galaxies, giving apparent magnitudes and colours in up to 160×160 pixels. We also obtain intrinsic and apparent integrated spectra and intrinsic colours of the model galaxies. All of these quantities can be calculated with a time resolution of 10 Myr. In the present work, they were calculated in time steps of 0.5 Gyr. We find that

1. The integrated colours of the model galaxy depend more strongly on the metallicity of the stars in the infrared ($(V - K)_0$, $(J - K)_0$, $V - K$, $J - K$) than in the optical and ultraviolet.
2. In the ultraviolet ($(U - B)_0$, $U - B$), star formation blankets metallicity - and absorption effects.
3. In the infrared and optical, metallicity effects are crucial for $z > 1.5$; at lower redshifts absorption becomes more important than metallicity. Thus both the metallicity distribution of the stars and the internal absorption by gas must be taken into account when deriving colours from galaxy models.
4. At low redshifts, bulge colours depend on the inclination of the model galaxy due to absorption from

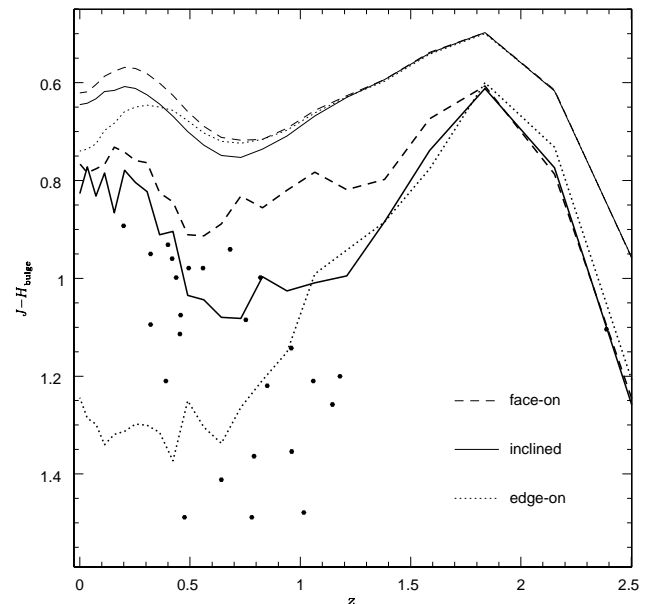


Fig. 14. Predicted bulge $J - H$ colours (thick lines) as function of redshift from the accretion model for three different inclinations (dashed: face-on, solid: inclined by 60° , dotted: edge-on), compared to HDF disk galaxy bulge colours (Ellis et al., 2001), transformed into the standard system according to Stephens et al. (2000) (thick points). The integrated model colours for the three inclinations are shown as thin lines.

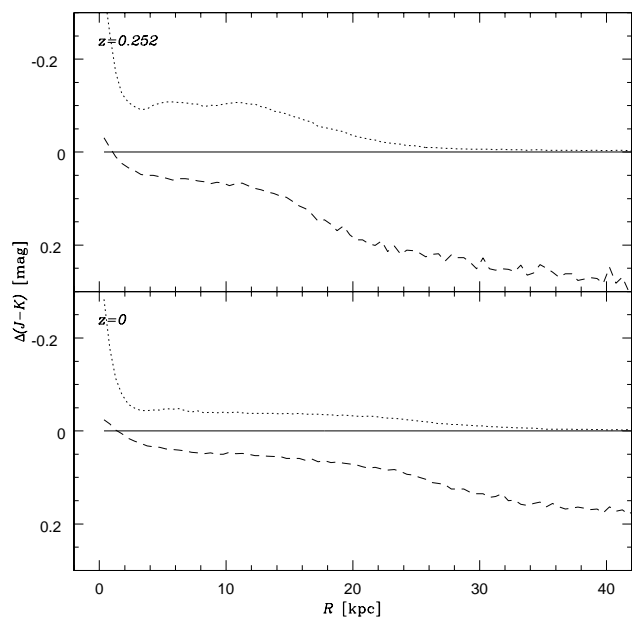


Fig. 17. Differences in the $J - K$ radial profiles between the solar metallicity model (dashed) resp. the absorptionless model (dotted) and the regular accretion model from Fig. 16, in the sense solar metallicity (absorptionless) - regular model. The solid line represents zero difference.

the disk. In our model, bulges are up to 0.5^m redder in edge-on projection than when seen face-on, which however is an upper limit because of the limited spatial resolution of the underlying numerical model.

5. We confirm the usefulness of m_K as a mass tracer, and find indications that metallicity gradients manifest themselves in $J-K$ (at low redshift), which would give us a means to measure $[\text{Fe}/\text{H}]$ gradients from $J-K$ gradients, if confirmed observationally.
6. A comparison of our model colours for disk galaxy bulges with empirical data from the HDF North (Ellis et al., 2001) shows good agreement, confirming that the star formation history and time dependent gas density distribution of the models are realistic.

The produced colour images and spectra have not been fully exploited yet by far. There is still a lot more information to extract and a lot more conclusions to be drawn from these files. This will be done in future work.

Our result that internal absorption is crucial at $z < 1.5$ shows that it is necessary in any galaxy formation model to have a realistic description of the gas component, if galaxy colours are to be predicted reliably. This requires at least a 2-phase model of the interstellar matter in which a cold star-forming medium coexists with a hot component which absorbs most of the energy and metal return from massive stars, i.e., a chemo-dynamical approach. Three-dimensional and high-resolution chemo-dynamical models, when embedded in a realistic cosmological model, allow us not only to predict the detailed morphology and colours of forming galaxies, but also to investigate the physical processes relevant during the formation and evolution of galaxies. Much further work on improving the present models is needed, but will be very rewarding.

The spectro-photometric programme that transforms the quantities calculated by the galaxy models into spectral properties has great potential, as it calculates colours and spectra in a realistic way including, e.g., spatially resolved absorption, using as few simplifications and assumptions as possible. Improvements of the input ingredients (the stellar evolutionary tracks, the stellar library, the absorption law) can easily be implemented. Other possible improvements are the inclusion of emission from HII regions and planetary nebulae, or the inclusion of supernovae spectra. The results do not need to be restricted to the *UBVRIJHKLM* system. Two dimensional distributions can in principle be calculated in any colour system, or for other spectral properties, such as line strength indices.

Acknowledgements. This work was supported by the Swiss National Science Foundation.

References

Abraham, R.G., Ellis, R.S., Fabian, A.C., Tanvir, N.R., & Glazebrook, K. 1999a, MNRAS, 303, 641
 Abraham, R.G., Merrifield, M.R., Ellis, R.S., Tanvir, N.R., & Brinchmann, J. 1999b, MNRAS, 308, 569

Appenzeller, I., Bender, R., Bohm, A. et al. 2000, The Messenger 100, 44
 Arimoto, N., & Yoshii, Y. 1987, A&A, 173, 23
 Barger, A.J., Cowie, L.L., Trentham, N. Fulton, E., Hu, E.M., Songaila, A., & Hall, D. 1999, AJ, 117, 102
 Barnes, J., & Efstathiou, G. 1987, ApJ, 319, 575
 Bekki, K., & Chiba, M., 2001 ApJ, 558, 666
 Berczik, P. 1999, A&A, 348, 371
 Bica, E. 1996 (private communication to T. Lejeune)
 Boissier, S., & Prantzos, N. 2001, MNRAS, 325, 321
 Bruzual A.G., & Charlot, S. 1993, ApJ, 405, 538
 Bruzual A.G., & Charlot, S. 2000, Galaxy isochrone spectral synthesis evolution library (private communication)
 Buser, R., & Kurucz, R.L. 1992, A&A, 264, 557 (BK)
 Campos, A., & Shanks, T. 1997, MNRAS, 291, 383
 Carroll, S.M., Press, W.H., & Turner, E.L. 1992 Annual Review of Astronomy and Astrophysics ,30, 499
 Charlot, S., & Bruzual, A.G. 1991, ApJ, 367, 126
 Cole, S., Lacey, C. 1996, MNRAS, 281, 716
 Cole, S., Lacey, C.G., Baugh, C.M., & Frenk, C.S. 2000, MNRAS, 319, 168
 Contardo, G., Steinmetz, M., & Fritze-von Alvensleben, U. 1998, ApJ, 507, 497
 Diaferio, A., Kauffmann, G., Colberg, J.M., & White, S.D.M. 1999, MNRAS, 307, 537
 Efstathiou, G., Lake, G., & Negroponte J. 1982, MNRAS, 199, 1069
 Eggen, O.J., Lynden-Bell, D., & Sandage, A.R. 1962, ApJ, 136, 748
 Ellis, R.S., Abraham, R.G., & Dickinson, M. 2001, ApJ, 551, 111
 Fagotto F., Bressan A., Bertelli G., & Chiosi C. 1994, A&AS 105, 39
 Firmani, C., & Avila-Reese, V. 2000, MNRAS, 315, 457
 Fluks, M.A., Plez, B., The, P.S., de Winter, D., Westerlund, B.E., & Steenman, H.C. 1994, A&AS, 105, 311
 Fukugita, M., Shimasaku, K., & Ichikawa, T. 1995, PASP, 107, 945
 Gardner, J.P. 2001, ApJ, 557, 616
 Girardi L., Bressan A., Chiosi C., Bertelli G., & Nasi E. 1996, A&AS 117, 113
 Girardi, L., Bressan, A., Bertelli, G., & Chiosi, C. 2000, A&AS, 141, 371 ("Padova 2000" isochrones)
 Gronwall, C., & Koo, D.C. 1995, ApJ, 440L, 1
 Hultman, J., & Pharasyn, A. 1999, A&A, 347, 769
 Jimenez, R., Padoan, P., Matteucci, F., & Heavens, A.F. 1998, MNRAS, 299, 123
 Jimenez, R., Friaça, A.C.S., Dunlop, J.S., Terlevich, R.J., Peacock, J.A., & Nolan, L.A. 1999, MNRAS, 305L, 16
 Kajisawa, M., & Yamada, T. 2001, PASJ, 53, 833
 Katz, N., & Gunn, J.E 1991, ApJ, 377, 365
 Kauffmann, G., & Charlot, S. 1998a MNRAS, 294, 705
 Kauffmann, G., & Charlot, S. 1998b MNRAS, 297L, 23
 Kauffmann, G., Colberg, J.M., Diaferio, A., & White, S.D.M. 1999, MNRAS 303, 188
 Lejeune, T., Cuisinier, F., & Buser, R. 1997, A&AS, 125, 229

- Lejeune, T., Cuisinier, F., & Buser, R. 1998, *A&AS*, 130, 65
- Lerner, M.S., Sundin, M., & Thomasson, M. 1999, *A&A*, 344, 483
- Lilly, S., Schade, D., Ellis, R., Le Fevre, O., Brinchmann, J., Tresse, L., Abraham, R., Hammer, F., Crampton, D., Colless, M., Glazebrook, K., Mallen-Ornelas, G., & Broadhurst, T. 1998, *ApJ*, 500, 75
- Madau, P. 1995, *ApJ*, 441, 18
- Matteucci, F., & Tornambe, A. 1987, *A&A*, 185, 51
- Metcalfe, N., Shanks, T., Fong, R., & Jones, L.R. 1991, *MNRAS*, 249, 498
- Mo, H.J., Mao, S., & White, S.D.M. 1998, *MNRAS*, 295, 319
- Nagamine, K., Fukugita, M., Cen, R., & Ostriker, J.P. 2001, *ApJ*, 558, 497
- Navarro, J.F., Frenk, C.S., & White, S.D.M. 1995, *MNRAS*, 275, 56
- Navarro, J.F., & Steinmetz, M. 2000, *ApJ*, 538, 477
- Pearce, F.R., Jenkins, A., Frenk, C.S., White, S.D.M., Thomas, P.A., Couchman, H.M.P., Peacock, J.A., & Efstathiou, G. 2001, *MNRAS*, 326, 649
- Pentericci, L., McCarthy, P.J., Röttgering, H.J.A., Miley, G.K., van Breugel, W.J.M., & Fosbury, R. 2001, *ApJS* 135, 63
- Quillen, A.C., Yukita, M., 2001, *AJ*, 121, 2095
- Roche, N., Ratnatunga, K., Griffiths, R.E., Im, M., & Neuschaefer, L. 1996, *MNRAS*, 282, 1247
- Roche, N., Ratnatunga, K., Griffiths, R. E., Im, M., & Naim, A. 1998, *MNRAS*, 293, 157
- Samland, M., & Gerhard, O.E. 2002, *A&A*, (submitted)
- Samland, M., Hensler, G., & Theis, C.P. 1997, *ApJ*, 476, 544
- Simard, L., Koo, D.C., Faber, S.M., Sarajedini, V.L., Vogt, N.P., Phillips, A.C., Gebhardt, K., Illingworth, G.D., & Wu, K.L. 1999, *ApJ*, 519, 563
- Steinmetz, M., & Müller, E. 1995, *MNRAS*, 276, 549
- Steinmetz, M., & Bartelmann, M. 1995, *MNRAS*, 272, 570
- Stephens, A.W., Frogel, J.A., Ortolani, S., Davies, R., Jablonka, P., Renzini, A., & Rich, R.M. 2000, *AJ*, 119, 419
- Thompson, R.I., Storrie-Lombardi, L.J., Weymann, R.J., Rieke, M.J., Schneider, G., Stobie, E., & Lytle, D. 1999, *AJ*, 117, 17
- van den Bosch, F.C. 1998, *ApJ*, 507, 601
- Vogt, N.P., Forbes, D.A., Phillips, A.C., Gronwall, C., Faber, S.M., Illingworth, G.D., & Koo, D.C. 1996, *ApJL* 465, L15
- Weil, M.L., Eke, V.R., & Efstathiou, G. 1998, *MNRAS*, 300, 773
- Westera, P. 2001, *The BaSeL 3.1 models: Metallicity calibration of a theoretical stellar spectral library and its application to chemo-dynamical galaxy models*, PhD thesis, Univ. of Basel, 378 pp.
- Westera, P., Lejeune, T., Buser, R., Cuisinier, F., & Bruzual A.G. 2002, *A&A*, 381, 524
- Williams, R.E., Blacker, B., Dickinson, M. et al. 1996, *AJ*, 112, 1335
- Williams, R.E., Baum, S., Bergeron, L.E. et al. 2000, *AJ*, 120, 2735
- Williams, P.R., & Nelson, A.H. 2001, *A&A*, 374, 839
- Zepf, S.E. 1997, *Nat.*, 390, 377

Appendix A: Intrinsic magnitudes and colours

Appendix B: Bulge colours

Table A.1. Intrinsic integrated magnitudes and colours of the accretion model.

z	$t[\text{Gyr}]$	M_{Bol}	M_U	M_V	M_K	$(U - B)_0$	$(B - V)_0$
4.035	1.5	-19.663	-18.451	-17.859	-18.672	-0.550	-0.042
3.150	2.0	-20.155	-19.077	-18.624	-19.516	-0.469	0.016
2.569	2.5	-21.015	-19.961	-19.581	-20.601	-0.439	0.059
2.153	3.0	-21.970	-20.899	-20.568	-21.686	-0.418	0.087
1.837	3.5	-22.663	-21.646	-21.385	-22.634	-0.387	0.126
1.586	4.0	-23.190	-22.202	-22.001	-23.452	-0.365	0.164
1.382	4.5	-23.430	-22.465	-22.355	-24.091	-0.326	0.216
1.211	5.0	-23.568	-22.571	-22.528	-24.537	-0.299	0.256
1.065	5.5	-23.606	-22.589	-22.642	-24.847	-0.252	0.305
0.939	6.0	-23.658	-22.601	-22.714	-25.048	-0.226	0.339
0.828	6.5	-23.696	-22.612	-22.781	-25.185	-0.200	0.369
0.730	7.0	-23.709	-22.603	-22.817	-25.273	-0.180	0.394
0.642	7.5	-23.726	-22.593	-22.838	-25.326	-0.168	0.413
0.562	8.0	-23.755	-22.616	-22.879	-25.374	-0.161	0.424
0.489	8.5	-23.786	-22.634	-22.903	-25.409	-0.162	0.431
0.423	9.0	-23.807	-22.645	-22.938	-25.449	-0.151	0.444
0.362	9.5	-23.797	-22.625	-22.938	-25.469	-0.141	0.454
0.305	10.0	-23.819	-22.636	-22.968	-25.500	-0.133	0.465
0.252	10.5	-23.801	-22.610	-22.964	-25.514	-0.123	0.477
0.203	11.0	-23.802	-22.594	-22.968	-25.529	-0.114	0.488
0.157	11.5	-23.777	-22.552	-22.945	-25.525	-0.106	0.499
0.113	12.0	-23.779	-22.547	-22.961	-25.536	-0.095	0.509
0.073	12.5	-23.760	-22.522	-22.945	-25.526	-0.092	0.515
0.034	13.0	-23.755	-22.495	-22.943	-25.529	-0.081	0.529
0.000	13.5	-23.709	-22.437	-22.911	-25.515	-0.067	0.541

Table A.2. Intrinsic integrated magnitudes and colours of the accretion model (part 2).

z	$(V - I)_0$	$(V - K)_0$	$(R - I)_0$	$(J - H)_0$	$(H - K)_0$	$(J - K)_0$	$(K - L)_0$	$(K - M)_0$
4.035	0.288	0.813	0.173	0.312	0.111	0.424	0.120	0.545
3.150	0.335	0.892	0.187	0.315	0.106	0.422	0.151	0.582
2.569	0.376	1.020	0.207	0.343	0.106	0.448	0.145	0.585
2.153	0.400	1.118	0.220	0.367	0.111	0.478	0.133	0.583
1.837	0.435	1.249	0.240	0.393	0.117	0.510	0.129	0.598
1.586	0.483	1.451	0.270	0.438	0.137	0.575	0.136	0.660
1.382	0.553	1.736	0.312	0.501	0.179	0.680	0.159	0.796
1.211	0.611	2.009	0.344	0.568	0.232	0.801	0.199	0.976
1.065	0.669	2.205	0.376	0.609	0.260	0.869	0.220	1.075
0.939	0.711	2.334	0.397	0.634	0.275	0.910	0.230	1.131
0.828	0.743	2.404	0.413	0.645	0.275	0.921	0.229	1.139
0.730	0.774	2.456	0.428	0.649	0.268	0.917	0.223	1.128
0.642	0.797	2.488	0.439	0.652	0.261	0.913	0.217	1.115
0.562	0.809	2.495	0.445	0.650	0.253	0.903	0.211	1.095
0.489	0.818	2.506	0.450	0.650	0.249	0.900	0.208	1.086
0.423	0.832	2.511	0.456	0.646	0.239	0.886	0.199	1.060
0.362	0.843	2.531	0.462	0.649	0.240	0.889	0.200	1.065
0.305	0.854	2.532	0.467	0.645	0.232	0.877	0.193	1.043
0.252	0.866	2.550	0.473	0.647	0.232	0.878	0.193	1.044
0.203	0.877	2.561	0.478	0.646	0.228	0.874	0.190	1.036
0.157	0.887	2.580	0.483	0.649	0.231	0.880	0.194	1.046
0.113	0.894	2.575	0.486	0.644	0.224	0.868	0.187	1.024
0.073	0.899	2.581	0.488	0.646	0.224	0.870	0.189	1.029
0.034	0.912	2.586	0.494	0.642	0.217	0.859	0.181	1.008
0.000	0.920	2.604	0.498	0.645	0.219	0.864	0.183	1.015

Table A.4. Apparent integrated magnitudes and colours of the accretion model.

z	$m - M$	m_{Bol}	m_U	m_V	m_K	$U - B$	$B - V$
4.035	47.795	31.921	39.855	32.253	29.668	5.177	2.425
3.150	47.153	30.267	32.478	30.281	28.211	1.543	0.654
2.569	46.619	28.489	28.484	28.708	26.559	-0.473	0.249
2.153	46.153	26.778	26.639	27.229	24.958	-0.633	0.043
1.837	45.731	25.398	25.276	26.058	23.591	-0.810	0.028
1.586	45.338	24.259	24.246	25.128	22.425	-0.902	0.020
1.382	44.969	23.453	23.677	24.547	21.494	-0.877	0.007
1.211	44.615	22.791	23.195	24.047	20.765	-0.904	0.052
1.065	44.269	22.253	22.879	23.646	20.124	-0.928	0.161
0.939	43.931	21.721	22.520	23.193	19.557	-0.914	0.241
0.828	43.595	21.216	22.200	22.746	19.012	-0.866	0.320
0.730	43.258	20.745	21.895	22.299	18.497	-0.797	0.393
0.642	42.918	20.272	21.543	21.830	18.013	-0.723	0.436
0.562	42.567	19.783	21.131	21.281	17.523	-0.652	0.502
0.489	42.203	19.284	20.667	20.679	17.037	-0.610	0.598
0.423	41.828	18.789	20.211	20.048	16.529	-0.574	0.737
0.362	41.430	18.305	19.757	19.418	16.036	-0.525	0.864
0.305	40.997	17.756	19.210	18.768	15.513	-0.482	0.924
0.252	40.522	17.209	18.666	18.159	14.992	-0.414	0.921
0.203	39.993	16.592	18.052	17.514	14.432	-0.332	0.870
0.157	39.375	15.914	17.375	16.810	13.818	-0.240	0.805
0.113	38.600	15.053	16.502	15.915	13.031	-0.141	0.728
0.073	37.592	13.985	15.405	14.833	12.036	-0.067	0.639
0.034	35.872	12.190	13.562	13.023	10.322	-0.035	0.574
0.000	25.000 ¹	1.291	2.563	2.089	-0.515	-0.067	0.541

¹To calculate apparent magnitudes for the zero redshift model, a distance modulus of 25 was chosen, corresponding to a distance of 1Mpc.

Table A.5. Apparent integrated magnitudes and colours of the accretion model (part 2).

z	$V-I$	$V-K$	$R-I$	$J-H$	$H-K$	$J-K$	$K-L$	$K-M$
4.035	1.128	2.585	0.461	0.326	0.928	1.254	0.640	2.411
3.150	0.353	2.070	0.149	0.896	0.517	1.412	0.772	2.578
2.569	0.261	2.149	0.157	1.022	0.465	1.487	0.771	2.640
2.153	0.252	2.271	0.151	0.617	0.522	1.139	0.707	2.320
1.837	0.315	2.467	0.211	0.498	0.519	1.016	0.714	2.278
1.586	0.425	2.703	0.289	0.540	0.548	1.089	0.771	2.370
1.382	0.568	3.053	0.346	0.594	0.615	1.209	0.859	2.540
1.211	0.730	3.282	0.448	0.630	0.659	1.289	0.964	2.665
1.065	1.073	3.522	0.725	0.668	0.675	1.342	1.043	2.683
0.939	1.302	3.636	0.887	0.709	0.662	1.371	1.044	2.594
0.828	1.429	3.734	0.912	0.736	0.648	1.384	0.998	2.530
0.730	1.464	3.802	0.835	0.753	0.644	1.397	0.913	2.528
0.642	1.473	3.817	0.738	0.749	0.642	1.391	0.822	2.389
0.562	1.418	3.758	0.621	0.728	0.647	1.375	0.707	2.189
0.489	1.314	3.642	0.543	0.700	0.660	1.360	0.561	2.065
0.423	1.209	3.519	0.526	0.669	0.674	1.343	0.405	1.982
0.362	1.088	3.382	0.528	0.644	0.685	1.329	0.320	1.911
0.305	1.003	3.255	0.518	0.625	0.663	1.288	0.272	1.766
0.252	0.962	3.167	0.511	0.612	0.630	1.241	0.250	1.633
0.203	0.943	3.082	0.510	0.608	0.578	1.186	0.215	1.530
0.157	0.925	2.992	0.503	0.616	0.516	1.132	0.188	1.476
0.113	0.919	2.884	0.500	0.618	0.443	1.061	0.155	1.356
0.073	0.919	2.797	0.492	0.633	0.374	1.007	0.155	1.245
0.034	0.925	2.701	0.495	0.642	0.289	0.931	0.165	1.097
0.000	0.920	2.604	0.498	0.645	0.219	0.864	0.183	1.015

Table A.6. Intrinsic integrated magnitudes and colours of the collapse model.

z	$t[Gyr]$	M_{Bol}	M_U	M_V	M_K	$(U-B)_0$	$(B-V)_0$
4.035	1.5	-20.964	-19.421	-18.541	-18.950	-0.734	-0.146
3.150	2.0	-24.454	-23.270	-22.728	-23.649	-0.544	0.002
2.569	2.5	-24.683	-23.743	-23.541	-25.065	-0.370	0.168
2.153	3.0	-24.674	-23.715	-23.675	-25.722	-0.299	0.259
1.837	3.5	-24.441	-23.445	-23.592	-25.958	-0.198	0.345
1.586	4.0	-24.292	-23.217	-23.522	-26.047	-0.120	0.425
1.382	4.5	-24.181	-23.022	-23.439	-26.068	-0.072	0.489
1.211	5.0	-24.087	-22.852	-23.331	-26.016	-0.055	0.534
1.065	5.5	-23.976	-22.683	-23.241	-25.958	-0.019	0.577
0.939	6.0	-23.883	-22.542	-23.155	-25.893	0.004	0.609
0.828	6.5	-23.787	-22.403	-23.067	-25.828	0.027	0.637
0.730	7.0	-23.713	-22.280	-22.990	-25.765	0.048	0.662
0.642	7.5	-23.635	-22.167	-22.912	-25.701	0.064	0.681
0.562	8.0	-23.565	-22.072	-22.853	-25.643	0.083	0.698
0.489	8.5	-23.494	-21.970	-22.779	-25.579	0.097	0.712
0.423	9.0	-23.440	-21.900	-22.729	-25.527	0.107	0.722
0.362	9.5	-23.381	-21.824	-22.672	-25.471	0.117	0.731
0.305	10.0	-23.335	-21.766	-22.622	-25.416	0.121	0.735
0.252	10.5	-23.271	-21.682	-22.563	-25.366	0.135	0.746
0.203	11.0	-23.231	-21.629	-22.522	-25.328	0.141	0.752
0.157	11.5	-23.196	-21.589	-22.485	-25.288	0.143	0.753
0.113	12.0	-23.157	-21.536	-22.443	-25.253	0.149	0.758
0.073	12.5	-23.126	-21.492	-22.412	-25.226	0.157	0.763
0.034	13.0	-23.088	-21.445	-22.374	-25.196	0.163	0.766
0.000	13.5	-23.067	-21.416	-22.350	-25.170	0.166	0.768

Table A.9. Apparent integrated magnitudes and colours of the collapse model.

z	$m - M$	m_{Bol}	m_U	m_V	m_K	$U - B$	$B - V$
4.035	47.795	30.731	38.131	30.816	28.890	4.998	2.317
3.150	47.153	25.972	28.040	25.876	24.102	1.479	0.685
2.569	46.619	24.766	25.160	25.137	22.562	-0.313	0.336
2.153	46.153	24.008	24.412	24.781	21.717	-0.481	0.112
1.837	45.731	23.563	24.193	24.808	21.118	-0.714	0.099
1.586	45.338	23.113	24.070	24.791	20.527	-0.812	0.091
1.382	44.969	22.669	23.973	24.646	19.988	-0.770	0.097
1.211	44.615	22.249	23.684	24.325	19.530	-0.817	0.176
1.065	44.269	21.867	23.532	24.024	19.107	-0.851	0.359
0.939	43.931	21.484	23.325	23.620	18.719	-0.825	0.530
0.828	43.595	21.115	23.155	23.214	18.347	-0.744	0.685
0.730	43.258	20.733	22.911	22.764	17.971	-0.644	0.791
0.642	42.918	20.357	22.671	22.321	17.607	-0.499	0.849
0.562	42.567	19.967	22.396	21.830	17.221	-0.338	0.904
0.489	42.203	19.571	22.034	21.304	16.835	-0.231	0.961
0.423	41.828	19.153	21.591	20.719	16.421	-0.164	1.036
0.362	41.430	18.718	21.129	20.109	16.001	-0.090	1.110
0.305	40.997	18.239	20.531	19.466	15.569	-0.096	1.161
0.252	40.522	17.738	19.963	18.833	15.120	-0.059	1.189
0.203	39.993	17.162	19.285	18.159	14.619	-0.032	1.158
0.157	39.375	16.495	18.511	17.402	14.045	0.003	1.106
0.113	38.600	15.674	17.612	16.518	13.309	0.069	1.025
0.073	37.592	14.618	16.478	15.420	12.331	0.130	0.928
0.034	35.872	12.857	14.619	13.617	10.653	0.166	0.836
0.000	25.000 ¹	1.933	3.584	2.650	-0.170	0.166	0.768

¹To calculate apparent magnitudes for the zero redshift model, a distance modulus of 25 was chosen, corresponding to a distance of 1Mpc.

Table A.10. Apparent integrated magnitudes and colours of the collapse model (part 2).

z	$V-I$	$V-K$	$R-I$	$J-H$	$H-K$	$J-K$	$K-L$	$K-M$
4.035	1.013	1.926	0.399	0.189	0.629	0.819	0.455	1.687
3.150	0.302	1.774	0.129	0.741	0.490	1.232	0.749	2.408
2.569	0.237	2.575	0.114	1.127	0.577	1.704	0.973	3.217
2.153	0.320	3.064	0.231	0.830	0.689	1.519	1.098	3.321
1.837	0.560	3.690	0.432	0.770	0.739	1.509	1.148	3.481
1.586	0.862	4.264	0.594	0.819	0.799	1.618	1.160	3.522
1.382	1.113	4.658	0.677	0.847	0.841	1.688	1.160	3.473
1.211	1.286	4.795	0.743	0.855	0.845	1.700	1.163	3.316
1.065	1.597	4.917	0.955	0.864	0.814	1.678	1.152	3.108
0.939	1.775	4.901	1.064	0.877	0.767	1.644	1.083	2.847
0.828	1.889	4.867	1.109	0.885	0.724	1.609	0.997	2.697
0.730	1.906	4.793	1.067	0.875	0.691	1.567	0.895	2.615
0.642	1.911	4.714	0.992	0.851	0.669	1.520	0.801	2.450
0.562	1.866	4.609	0.889	0.811	0.662	1.473	0.674	2.252
0.489	1.785	4.469	0.807	0.766	0.672	1.438	0.518	2.116
0.423	1.686	4.298	0.756	0.719	0.687	1.406	0.360	2.004
0.362	1.566	4.108	0.732	0.679	0.693	1.372	0.254	1.886
0.305	1.437	3.897	0.689	0.647	0.673	1.319	0.205	1.748
0.252	1.337	3.713	0.660	0.622	0.635	1.257	0.185	1.618
0.203	1.259	3.540	0.638	0.611	0.579	1.189	0.169	1.510
0.157	1.183	3.357	0.614	0.612	0.508	1.120	0.160	1.421
0.113	1.148	3.209	0.600	0.622	0.434	1.055	0.150	1.306
0.073	1.127	3.089	0.578	0.637	0.358	0.995	0.145	1.182
0.034	1.114	2.964	0.574	0.655	0.278	0.932	0.154	1.067
0.000	1.090	2.820	0.572	0.655	0.201	0.856	0.167	0.984

Table B.1. Bulge colours of the accretion model, face-on.

z	$U-B$	$B-V$	$V-I$	$V-K$	$R-I$	$J-H$	$H-K$	$J-K$	$K-L$	$K-M$
4.035	5.411	2.515	1.182	2.809	0.490	0.374	1.006	1.380	0.659	2.582
3.150	2.013	0.819	0.569	2.889	0.240	1.166	0.605	1.771	0.837	3.038
2.569	-0.176	0.571	0.571	3.508	0.328	1.333	0.634	1.966	0.883	3.308
2.153	-0.354	0.195	0.449	3.194	0.275	0.787	0.649	1.436	0.881	2.897
1.837	-0.691	0.081	0.512	3.053	0.397	0.607	0.615	1.222	0.915	2.795
1.586	-0.808	0.033	0.771	3.585	0.504	0.674	0.722	1.395	1.021	3.056
1.382	-0.869	-0.070	0.889	4.071	0.470	0.798	0.951	1.749	1.266	3.697
1.211	-0.867	0.249	1.340	4.764	0.691	0.819	0.964	1.783	1.315	3.673
1.065	-0.863	0.302	1.369	4.348	0.863	0.783	0.853	1.637	1.220	3.208
0.939	-0.764	0.570	1.881	4.777	1.136	0.820	0.761	1.581	1.095	2.821
0.828	-0.732	0.703	1.932	4.714	1.143	0.856	0.742	1.598	1.045	2.753
0.730	-0.843	0.352	1.416	3.926	0.848	0.832	0.746	1.577	1.065	2.891
0.642	-0.759	0.522	1.636	4.319	0.846	0.889	0.757	1.645	0.973	2.817
0.562	-0.641	0.606	1.644	4.474	0.760	0.913	0.772	1.684	0.847	2.679
0.489	-0.550	0.688	1.569	4.481	0.682	0.911	0.789	1.700	0.670	2.589
0.423	-0.578	0.737	1.458	4.289	0.648	0.844	0.779	1.623	0.457	2.388
0.362	-0.438	0.929	1.392	4.265	0.659	0.825	0.805	1.630	0.349	2.326
0.305	-0.493	0.949	1.202	3.933	0.599	0.764	0.769	1.533	0.278	2.106
0.252	-0.461	0.961	1.107	3.857	0.577	0.759	0.763	1.521	0.279	2.041
0.203	-0.391	0.938	1.071	3.757	0.574	0.742	0.710	1.452	0.256	1.925
0.157	-0.385	0.805	0.963	3.515	0.532	0.732	0.632	1.364	0.234	1.805
0.113	-0.289	0.731	0.980	3.540	0.544	0.767	0.585	1.352	0.235	1.768
0.073	-0.062	0.744	1.065	3.556	0.569	0.776	0.495	1.271	0.218	1.609
0.034	0.071	0.699	1.086	3.443	0.579	0.784	0.398	1.182	0.229	1.451
0.000	-0.049	0.586	1.034	3.199	0.566	0.766	0.298	1.064	0.238	1.304

Table B.2. Bulge colours of the accretion model, edge-on.

z	$U - B$	$B - V$	$V - I$	$V - K$	$R - I$	$J - H$	$H - K$	$J - K$	$K - L$	$K - M$
4.035	5.574	2.562	1.211	2.911	0.504	0.395	1.038	1.433	0.671	2.640
3.150	2.332	0.868	0.623	3.047	0.263	1.207	0.620	1.827	0.849	3.104
2.569	-0.295	0.471	0.497	3.304	0.289	1.298	0.628	1.926	0.882	3.280
2.153	-0.521	0.102	0.334	2.758	0.209	0.732	0.619	1.350	0.857	2.796
1.837	-0.706	0.063	0.499	2.956	0.398	0.600	0.618	1.218	0.944	2.830
1.586	-0.782	-0.017	0.968	4.126	0.623	0.776	0.841	1.617	1.172	3.500
1.382	-0.816	-0.021	1.114	4.730	0.585	0.885	1.089	1.974	1.487	4.245
1.211	-0.955	0.109	1.038	4.731	0.563	0.942	1.190	2.133	1.705	4.666
1.065	-0.945	0.341	1.372	4.981	0.868	0.991	1.198	2.189	1.834	4.795
0.939	-0.906	0.805	1.768	5.531	1.088	1.151	1.202	2.353	1.818	4.785
0.828	-0.845	0.498	1.462	5.140	0.926	1.208	1.169	2.377	1.749	4.739
0.730	-0.596	0.669	1.737	5.595	0.960	1.264	1.252	2.516	1.814	5.135
0.642	-0.500	0.582	1.631	5.704	0.832	1.337	1.301	2.639	1.744	5.158
0.562	-0.553	0.511	1.532	5.598	0.723	1.304	1.276	2.580	1.558	4.830
0.489	-0.531	0.560	1.427	5.447	0.655	1.250	1.265	2.515	1.361	4.696
0.423	-0.304	0.891	1.533	6.062	0.736	1.373	1.414	2.787	1.280	4.893
0.362	-0.538	0.850	1.405	5.839	0.738	1.315	1.341	2.657	0.965	4.516
0.305	-0.213	1.174	1.456	5.956	0.780	1.300	1.322	2.622	0.909	4.406
0.252	-0.416	0.980	1.302	5.757	0.718	1.298	1.292	2.590	0.839	4.269
0.203	-0.393	0.881	1.267	5.740	0.705	1.313	1.262	2.575	0.831	4.194
0.157	-0.185	0.912	1.344	5.784	0.739	1.319	1.121	2.440	0.673	3.775
0.113	-0.247	0.753	1.327	5.768	0.744	1.340	1.066	2.406	0.678	3.748
0.073	0.161	0.891	1.498	5.742	0.814	1.298	0.883	2.181	0.538	3.149
0.034	0.194	0.884	1.636	5.797	0.898	1.286	0.773	2.059	0.557	2.917
0.000	0.030	0.830	1.644	5.551	0.920	1.244	0.629	1.872	0.503	2.623